Interplay between symmetric arginine dimethylation and ubiquitylation regulates TDP1 proteostasis for the repair of topoisomerase I-DNA adducts

Cell Reports

Article

Interplay between symmetric arginine dimethylation and ubiquitylation regulates TDP1 proteostasis for the repair of topoisomerase I-DNA adducts

Graphical abstract

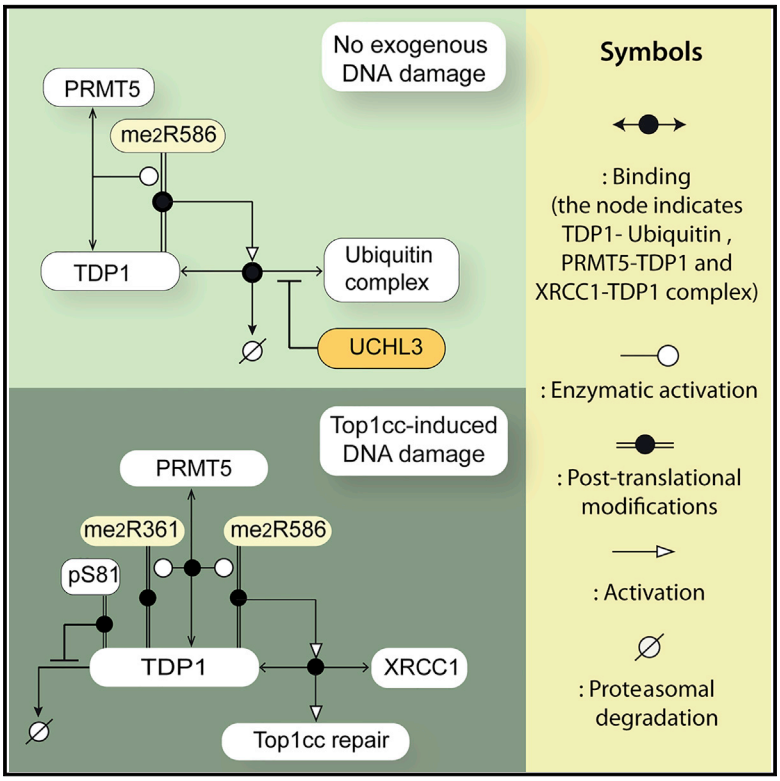

Highlights

- TDP1-R586 methylation promotes ubiquitin/proteasome-dependent TDP1 turnover
- TDP1-R586 promotes formation of XRCC1 repair foci at Top1cc-DNA damage sites
- TDP1 dimethylation at R361stimulates the 3′-phosphodiesterase activity of TDP1

Authors

Sangheeta Bhattacharjee, Ishita Rehman, Saini Basu, Souvik Nandy, Julia M. Richardson, Benu Brata Das

Correspondence

pcbbd@iacs.res.in

In brief

Bhattacharjee et al. identify a mechanism by which PRMT5 regulates Top1cc repair and genome stability by controlling the crosstalk between TDP1 arginine methylation and ubiquitylation, by binding with UCHL3, which is critical for TDP1 homeostasis and responses to Top1 poisons. *PRMT5 KO* cells show defective TDP1 proteostasis and increased CPT-induced cell death.

Bhattacharjee et al., 2022, Cell Reports *39*, 110940
June 14, 2022
https://doi.org/10.1016/j.celrep.2022.110940

CellPress

Cell Reports

CellPress
OPEN ACCESS

Article

Interplay between symmetric arginine dimethylation and ubiquitylation regulates TDP1 proteostasis for the repair of topoisomerase I-DNA adducts

Sangheeta Bhattacharjee,[1,3] Ishita Rehman,[1,3] Saini Basu,[1] Souvik Nandy,[1] Julia M. Richardson,[2] and Benu Brata Das[1,4,*]
[1]Laboratory of Molecular Biology, School of Biological Sciences, Indian Association for the Cultivation of Science, 2A & B, Raja S. C. Mullick Road, Jadavpur, Kolkata 700032, India
[2]Institute of Quantitative Biology, Biochemistry, and Biotechnology, School of Biological Sciences, University of Edinburgh, The King's Buildings, Max Born Crescent, Edinburgh EH9 3BF, UK
[3]These authors contributed equally
[4]Lead contact
*Correspondence: pcbbd@iacs.res.in
https://doi.org/10.1016/j.celrep.2022.110940

SUMMARY

Tyrosyl-DNA phosphodiesterase (TDP1) hydrolyzes the phosphodiester bond between a DNA 3′ end and a tyrosyl moiety and is implicated in the repair of trapped topoisomerase I (Top1)-DNA covalent complexes (Top1cc). Protein arginine methyltransferase 5 (PRMT5) catalyzes arginine methylation of TDP1 at the residues R361 and R586. Here, we establish mechanistic crosstalk between TDP1 arginine methylation and ubiquitylation, which is critical for TDP1 homeostasis and cellular responses to Top1 poisons. We show that R586 methylation promotes TDP1 ubiquitylation, which facilitates ubiquitin/proteasome-dependent TDP1 turnover by impeding the binding of UCHL3 (deubiquitylase enzyme) with TDP1. TDP1-R586 also promotes TDP1-XRCC1 binding and XRCC1 foci formation at Top1cc-damage sites. Intriguingly, R361 methylation enhances the 3′-phosphodiesterase activity of TDP1 in real-time fluorescence-based cleavage assays, and this was rationalized using structural modeling. Together, our findings establish arginine methylation as a co-regulator of TDP1 proteostasis and activity, which modulates the repair of trapped Top1cc.

INTRODUCTION

Proteome stability is ensured by a multi-compartmental system that coordinates the protein synthesis, folding, disaggregation, and degradation machinery. Together, these form the complex proteostasis network, which is critical for cellular functionality and genomic stability (Hipp et al., 2019; Labbadia and Morimoto, 2015). Cellular protein homeostasis is stringently regulated by the ubiquitin-proteasome system (UPS) (Ravid and Hochstrasser, 2008; Swatek and Komander, 2016), which is responsible for the degradation of most ubiquitylated proteins; how its activity is regulated remains poorly understood. An imbalance in protein degradation may lead to proteostasis collapse, which is responsible for the perturbation of cellular homeostasis leading to a myriad of human diseases (Groen and Gillingwater, 2015; Popovic et al., 2014).

Human TDP1 is a neuroprotective enzyme, and a homozygous mutation of TDP1 ($H^{493}R$) is responsible for the neurodegenerative syndrome spinocerebellar ataxia with axonal neuropathy (SCAN1) (Das et al., 2021; El-Khamisy, 2011; Ghosh et al., 2019; Interthal et al., 2005; Katyal et al., 2007; Kawale and Povirk, 2018; Pommier et al., 2014; Takashima et al., 2002). TDP1 typically hydrolyzes the phosphodiester bond between a DNA 3′end and a tyrosyl moiety that arises from the catalytic activity of DNA topoisomerase I (Top1) (Yang et al., 1996). Top1-mediated supercoiling relaxation requires the production of reversible Top1-linked DNA single-strand breaks (SSBs) (Top1cc), which are normally short-lived but are selectively trapped by the anticancer drug camptothecin (CPT) and its clinical derivatives (Capranico et al., 2017; Das et al., 2016; Pommier, 2006; Pommier et al., 2016). Unrepaired Top1cc are detrimental DNA lesions, as they generate DNA double-strand breaks (DSBs) and trigger cell-cycle arrest and cell death (Pommier et al., 2016; Sordet et al., 2009). Accordingly, genetic inactivation of TDP1 causes hypersensitivity to CPT and a broad range of DNA-damaging agents including ionizing radiations (IR) (Das et al., 2009, 2014; Hirano et al., 2007; Katyal et al., 2007; Kawale and Povirk, 2018; Murai et al., 2012).

Post-translational modifications of TDP1 are part of the DNA damage response that accounts for the subcellular localization, stability, and recruitment of TDP1 at DNA damage sites (Chiang et al., 2010; Das et al., 2009, 2014; Hudson et al., 2012; Kawale and Povirk, 2018; Liao et al., 2018; Pommier et al., 2014; Rehman et al., 2018). DNA damage increases the half-life of TDP1 through phosphorylation and PARylation (Chiang et al., 2010; Das et al., 2009, 2014; Chowdhuri and Das, 2021), and therefore, the ubiquitin-proteasome system plays an important role in regulating TDP1 turnover; UCHL3 was identified as the deubiquitylase

enzyme (DUB) controlling TDP1 proteostasis (Liao et al., 2018). Notably, aberrant accumulation of TDP1 levels is linked with chromosome instability in cancer (Duffy et al., 2016). Arginine methylation stimulates the 3′-phosphodiesterase activity of TDP1 and promotes cell survival in response to CPT and ionizing radiation (Rehman et al., 2018), but how TDP1-arginine methylation cross-talks with TDP1-ubiquitylation to regulate TDP1 turnover for genomic stability remains unknown.

Arginine methylation is a key post-translational modification responsible for the addition of the methyl group on about 0.5% of arginine residues in human proteins and is involved in the choreography of a variety of cellular events, including epigenetic regulation, DNA repair, and genome maintenance (Auclair and Richard, 2013; Bedford and Clarke, 2009; Guccione and Richard, 2019). Protein arginine methyltransferases (PRMTs) are enzymes that catalyze the transfer of methyl groups from *S*-adenosyl-L-methionine to the guanidine nitrogen of arginine residues. Protein arginine methyltransferase 5 (PRMT5) has emerged as a major symmetric dimethylating (SDMA) enzyme involved in methylation of a myriad of substrates, thereby potentially impacting multiple cellular signaling events and cell survival (Guccione and Richard, 2019; Karkhanis et al., 2011).

Human PRMT5 is an oncogenic driver that stimulates cell proliferation by adding SDMA marks on a range of acceptor proteins, including the core histones H3 and H4, non-histones, including p53, E2F1, and DNA repair proteins RUVBL1, 53BP1, FEN1, RAD9, and TDP1 for genome maintenance (Auclair and Richard, 2013; Cho et al., 2012; Guo et al., 2010; He et al., 2011; Jansson et al., 2008; Karkhanis et al., 2011; Yang and Bedford, 2013).

This study establishes the mechanistic crosstalk between TDP1 arginine methylation and ubiquitylation for TDP1 function and responses to Top1 inhibitors. We identify that TDP1 arginine methylation at R586 is a negative regulator of TDP1 stability and promotes ubiquitin/proteasome-dependent TDP1 turnover, which promotes the propagation of the DNA damage response through the recruitment of XRCC1 foci at DNA damage sites. We further show that R361 dimethylation enhances the 3′-phosphodiesterase activity of TDP1. Together, our findings provide mechanistic insight for TDP1 regulation through arginine methylation for the repair of trapped Top1cc.

RESULTS

PRMT5 knockout cells accumulate TDP1

Steady regulation of TDP1 expression is critical for genome maintenance and neurological functions (Liao et al., 2018). We have previously described that TDP1 is methylated by PRMT5 at R361 and R586, which is critical for Top1cc repair (Rehman et al., 2018). Therefore, to determine the functional relationship between PRMT5 and TDP1, we generated isogenic clones of the HCT116 cell line knockout for the *PRMT5* gene using the CRISPR-Cas9 system (Naito et al., 2015) (Figures S1A and S1B). First, we confirmed that PRMT5 knockout (*PRMT5 KO*) abrogated TDP1 arginine dimethylation (Figure 1A). We detected ~60%–70% of the immunoprecipitated TDP1 is arginine methylated in PRMT5-proficient cells (Figure S1C), as before (Rehman et al., 2018). Next, we measured the endogenous TDP1 protein levels both in stable *PRMT5 KO* and in PRMT5-proficient (*wild-type*) HCT116 cells (Figures 1B and 1C). Notably, upon *PRMT5* knockout (KO), we detected a significant increase in TDP1 level (~1-fold) even without DNA damage (Figure 1C), which was not reduced in cells after CPT treatment, implying a role for PRMT5 in optimizing TDP1 proteostasis. The increase of TDP1 expression in CPT-treated *wild-type* cells (Figure 1C) is consistent with previous reports (Chiang et al., 2010; Das et al., 2009, 2014; Chowdhuri and Das, 2021). To determine whether TDP1 expression was also transcriptionally regulated, we measured TDP1 mRNA expression in *PRMT5 KO* cells. Quantitative PCR analysis shows that, unlike the protein level, TDP1 mRNA levels were diminished in *PRMT5 KO* cells compared with that of *wild-type* cells (Figure 1D). CPT treatment did not increase but rather decreased the TDP1 mRNA levels as reported previously (Das et al., 2009; Zaksauskaite et al., 2021). This is consistent with *PRMT5 KO* cells, suggesting that the enhancement in TDP1 protein levels is due to modulations at the post-translational level (Figure 1D).

Next, we tested the biological significance of the increased levels of methylated defective TDP1 in *PRMT5 KO* cells. Intriguingly, we observed that *PRMT5 KO* resulted in accumulation of DNA breaks even without DNA damage, which was markedly increased by ~3-fold (as measured by alkaline comet assays) following 1 h of incubation with CPT compared with PRMT5 *wild-type* cells (Figure 1E). Subsequent cell survival experiments validated that the CPT-induced increase in DNA breaks in *PRMT5 KO* cells is linked with a marked increase in CPT-mediated cytotoxicity (Figure 1F). We further confirmed that complementation of TDP1 arginine methylation single mutants (R361K and R586K) or *wild-type* TDP1 failed to protect the CPT hypersensitivity of *PRMT5 KO* cells (Figure S1D). Next, under similar conditions, we expressed TDP1 containing the mutations R361F and R586F ($TDP1^{FF}$), which mimic arginine methylation, in *PRMT5 KO* ($PRMT5^{-/-}$) cells. We found that $PRMT5^{-/-\ TDP1^{FF}}$ cells were partly protected from CPT-mediated cytotoxicity compared with PRMT5-proficient cells (Figure 1F), suggesting that PRMT5 exhibits additional mechanisms for the repair of Top1cc independently of TDP1. Therefore, increased expression of TDP1 in *PRMT5 KO* cells failed to rescue CPT-induced cytotoxicity, suggesting that PRMT5-dependent TDP1 arginine dimethylation is linked with TDP1 turnover.

Arginine dimethylation regulates TDP1 stability

PRMT5-mediated arginine dimethylation of downstream target proteins like KLF4, 53BP1, and E2F1 regulates their turnover, stability, subcellular localization, activity, or molecular interactions (Cho et al., 2012; Guccione and Richard, 2019; Hu et al., 2015). To examine the role of PRMT5 in regulating endogenous TDP1 stability, experiments were carried out in the presence of the protein synthesis inhibitor cycloheximide (CHX) in *wild-type* and *PRMT5 KO* cells. In the absence of DNA damage, the half-life of endogenous TDP1 was markedly prolonged in *PRMT5 KO* cells (Figure 2A and the quantification in 2B). The relative extent of TDP1 accumulation was also increased after CPT-induced DNA damage (Figure 2C and the quantification in 2D) in *PRMT5 KO* cells, consistent with the increased TDP1 levels measured in *PRMT5 KO* cells after CPT treatment (Figure 1C).

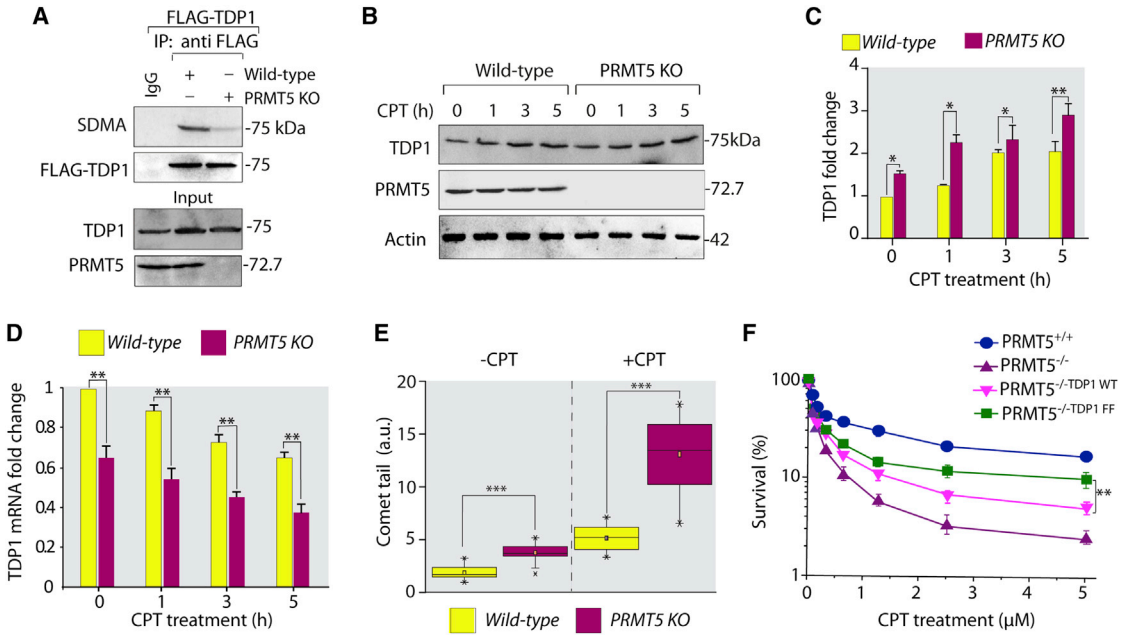

Figure 1. PRMT5 knockout enhances TDP1 protein levels

(A) Immunoprecipitation of ectopic FLAG-TDP1 using anti-FLAG antibody from *wild-type* and *PRMT5 KO* cells. The immune complexes were blotted with SDMA-specific antibodies and then stripped and re-probed with an anti-FLAG antibody to show equal loading.

(B and C) Induction of TDP1 expression in *PRMT5 KO* cells. A representative blot showing TDP1 and PRMT5 protein levels after treatment with CPT (5 μM) for the indicated times (h) from three independent experiments. Proteins were analyzed by western blotting (B) and quantified by densitometry normalized against actin (C). Error bars represent mean ± SEM (n = 3).

(D) The *wild-type* and *PRMT5 KO* cells were treated with CPT (5 μM) for the indicated times (h), and mRNA levels of TDP1 normalized to actin were analyzed and quantified by real-time PCR. Error bars represent mean ± SEM (n = 3).

(E) Alkaline comet assay showing increased induction of DNA strand breaks in *PRMT5 KO* cells compared with *wild-type* counterparts following CPT treatment. Comet tails were calculated for 25–30 cells by box-whisker plot using Origin software and show a significant difference (***p < 0.0001; t test).

(F) Cell survival curves of PRMT5$^{+/+}$, *PRMT5 KO* (PRMT5$^{-/-}$), and *PRMT5 KO* cells complemented with FLAG-tagged *wild-type* TDP1 (PRMT5$^{-/-\ TDP1\ WT}$), or TDP1 arginine methylation mimic double-mutant R361F and R586F [FF] (PRMT5$^{-/-\ TDP1\ FF}$) were exposed to CPT for 72 h. CPT-induced cytotoxicity (%) was calculated with respect to untreated cells. Error bars represent SD (n = 3). *Statistically significant differences: **p < 0.001; t test.

To further investigate the role of TDP1-arginine dimethylation in TDP1 stability, we measured the half-life of the exogenous polypeptides *wild-type* (WT) FLAG-tagged-TDP1^{WT} and the arginine dimethylation double mutant containing R361K and R586K (FLAG-TDP1^{KK}) in cells in the presence of CHX. Figure 2E shows that, in the absence of exogenous DNA damage, FLAG-TDP1^{KK} exhibits increased accumulation compared with FLAG-TDP1^{WT}. We further confirmed that FLAG-TDP1^{KK} failed to show CPT-induced accumulation (Figure 2F). The increased half-life of arginine methylation double-mutant FLAG-TDP1^{KK} parallels the increased stability of endogenous TDP1 in *PRMT5 KO* cells, further confirming that PRMT5-mediated arginine dimethylation regulates TDP1 turnover (Figures 2E and 2F). Notably, the increased stability of TDP1 after DNA damage is independent of the methylation sites (Figure 2F). Together, these results confirm that PRMT5-dependent TDP1 arginine dimethylation is linked with TDP1 turnover, which is independent of DNA damage.

R586 methylation promotes ubiquitin/proteasome-dependent TDP1 turnover

To examine the independent role of TDP1 dimethylation at residues R361 or R586 for imparting TDP1 stability, we measured the half-life of mutant TDP1 variants (FLAG-TDP1^{R361K} or FLAG-TDP1^{R586K}) by using CHX chase experiments. Figure 3A demonstrates that the R586 methylation mutant TDP1 shows an increased half-life compared with the R361-methylation mutant TDP1. Conversely, the disappearance pattern of methylation single-mutant TDP1^{R361K} parallels the wild-type TDP1 (compare Figures 3A and 2E). However, this difference was abrogated upon exogenous DNA damage with CPT (Figure 3B), consistent with the stability of methylation double-mutant TDP1 (R361K and R586K) in the presence of CPT (Figure 2F). Together, these results confirm that R586 dimethylation regulates TDP1 turnover in the absence of exogenous DNA damage.

Because TDP1 is ubiquitylated (Liao et al., 2018), this prompted us to investigate the role of the ubiquitin/proteasome system (UPS) and the arginine dimethylation axis in TDP1 proteostasis (Hipp et al., 2019). We confirmed the role of the proteasome for TDP1 degradation using proteasomal inhibitor MG132. Figure 3C shows that MG132 rescued the degradation of TDP1 in the presence of CHX, suggesting that TDP1 undergoes proteostasis through the proteasome-mediated pathway.

Next, we tested whether TDP1 dimethylation at R361 or R586 promotes TDP1 ubiquitylation. To that effect, we

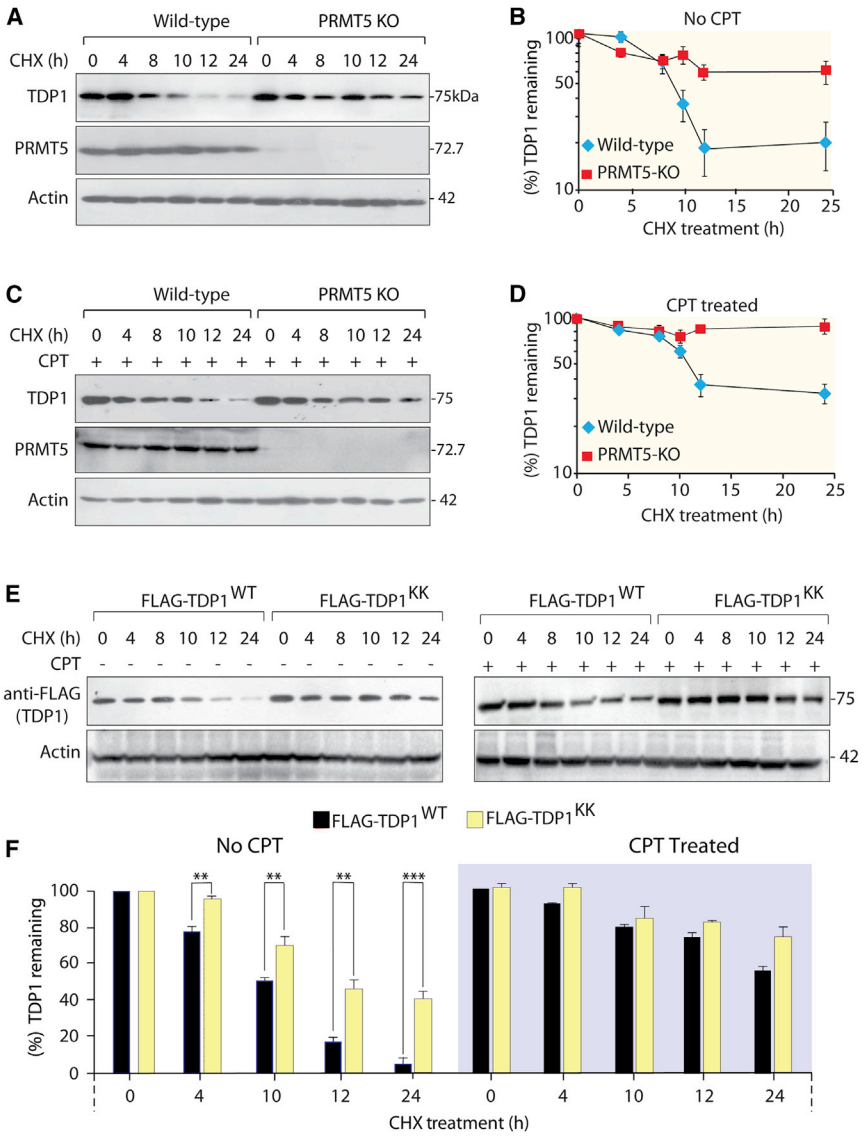

Figure 2. TDP1 is stabilized in *PRMT5 KO* cells

(A–D)The *wild-type* and *PRMT5 KO* cells were treated with cycloheximide (CHX) for the indicated time points (h) in the absence (no CPT, A), or presence of CPT (5 μM/3 h; C). The protein levels (TDP1 and PRMT5) were analyzed by western blotting (representative blots), and the relative level of TDP1 was quantified by densitometry normalized against actin. The remaining TDP1 level was calculated relative to levels before CHX treatment (B and D). Error bars represent mean ± SEM (n = 3).

(E) The increased stability of dimethylation mutant TDP1 is independent of DNA damage. HCT116 cells were transfected with FLAG-tagged wild-type (WT) or the double-mutant R361K and R586K [KK] TDP1 and 24 h later were treated with CHX for the indicated time points (h) in the absence (left), or presence of CPT (5 μM/3 h; right). Representative experiments show ectopic TDP1 levels as determined by western blotting with anti-FLAG antibody.

(F) Densitometry analysis of $TDP1^{WT}$ and $TDP1^{KK}$ levels in the presence and absence of CPT normalized against actin; the remaining TDP1 level was calculated relative to levels before CHX treatment. Error bars represent mean ± SEM (n = 3). **p < 0.001, ***p < 0.0001; t test.

performed pull-down experiments in cells transfected with plasmids encoding the FLAG-tagged TDP1 variants (WT, R361K, and R586K) and a HA-tagged ubiquitin in the presence or absence of CPT, as shown in Figure 3C. We confirmed that wild-type TDP1 co-immunoprecipitated ubiquitylated TDP1 (Ub-TDP1) as detected by slower migrating Ub-TDP1 bands, consistent with previous reports (Liao et al., 2018) (Figure 3D, Ub-TDP1; see the quantification in Figure 3E). We also noticed that TDP1 ubiquitylation was significantly reduced after CPT treatment (Figures 3D and 3E), which confirmed the increased stability of TDP1 after DNA damage was associated with $TDP1^{S81}$ phosphorylation (Figures S4A and S4B) (Das et al., 2009). Notably, the R586 methylation TDP1 mutant ($TDP1^{R586K}$) was markedly deficient in pulling down HA-ubiquitin compared with its wild-type ($TDP1^{WT}$) or R361 methylation mutant TDP1 ($TDP1^{R361K}$) in the presence or absence of CPT treatment (Figure 3D). Accordingly, we detected a marked reduction in the ubiquitylated TDP1 (Ub-TDP1) in both the presence and the absence of CPT (Figure 3D, Ub-TDP1; see the quantification in Figure 3E). We have further confirmed these results independently in HEK293 cells (Figure S2A), suggesting that the defective ubiquitylation of R586 methylation mutant TDP1 ($TDP1^{R586K}$) is independent of cell types or DNA damage response (Figure 3E). Furthermore, both $TDP1^{WT}$ and the methylation mutant $TDP1^{R361K}$ pull down similar levels of ubiquitylated TDP1 in the presence or absence of DNA damage (Figure 3E), confirming that R586 methylation facilitates TDP1 ubiquitylation.

Deubiquitylases (DUB) remove conjugated ubiquitin chains from substrate proteins, rescuing them from degradation or modulating ubiquitin-mediated signal transduction (Clague et al., 2019). UCHL3 is a DUB that binds to TDP1 and has been implicated in the reduction of ubiquitylated TDP1 (Liao et al., 2018). Therefore, we tested whether arginine methylation of TDP1 regulates its interaction with UCHL3. Immunoprecipitation of ectopic FLAG-TDP1 variants (WT, R361K, or R586K) showed a marked increase in the interaction of endogenous UCHL3 with ectopic R586K mutant TDP1, both in the presence and in the absence of DNA damage (Figure 3D, UCHL3, and 3F and Figures S2B and S2C). The increased interaction of the DUB (UCHL3) with $TDP1^{R586K}$ is in keeping with the decreased binding of ubiquitin with FLAG-$TDP1^{R586K}$ (Figure 3E, Ub-TDP1). Unlike the methylation

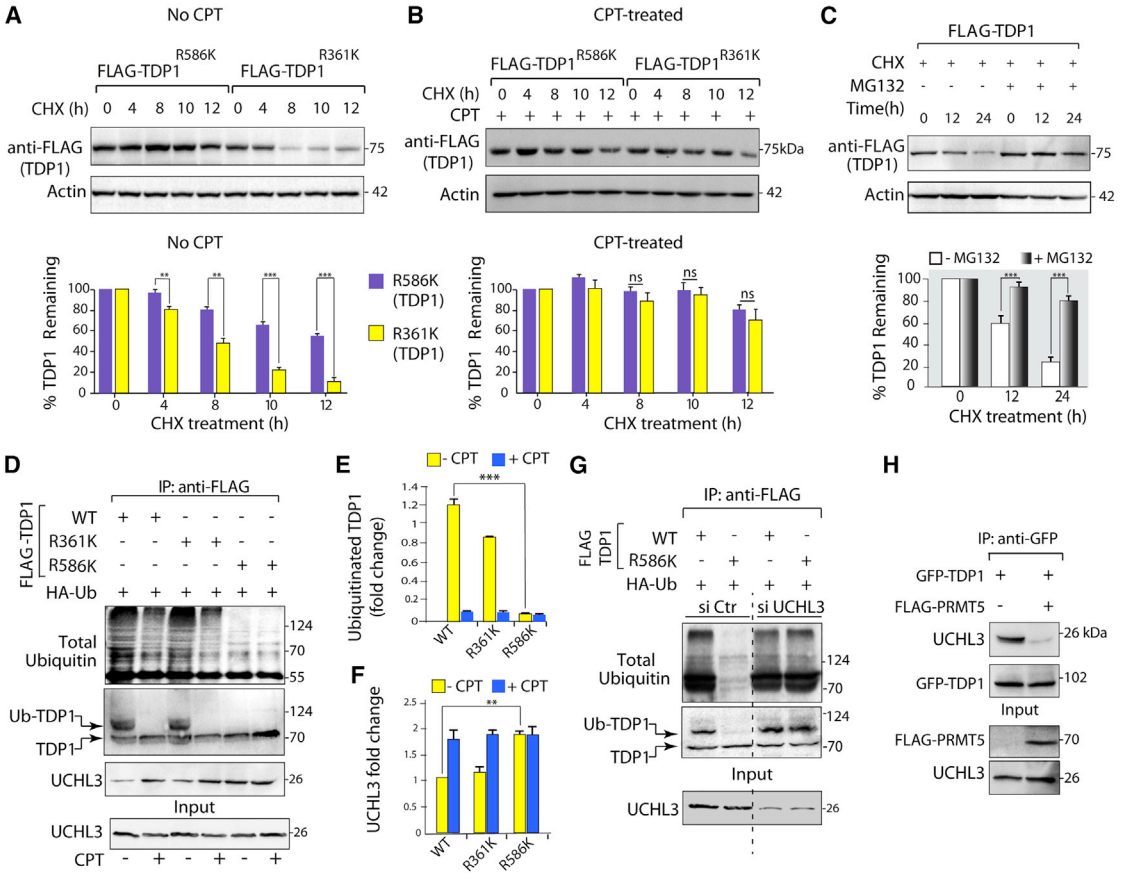

Figure 3. R586 dimethylation promotes ubiquitin-dependent TDP1 proteostasis

(A and B) Representative blots showing that TDP1^{R586K} exhibits increased half-life compared with TDP1^{R361K} in the absence of CPT. HCT116 cells were transfected with FLAG-TDP1^{R586K} or FLAG-TDP1^{R361K} and later treated with CHX for the indicated time points in the absence (A, top), or in the presence of CPT (5 μM/3 h; B, bottom). FLAG-tagged TDP1 levels (A and B, bottom) were determined by western blotting and quantified by densitometry normalized to actin, and the remaining TDP1 level was calculated relative to levels before CHX treatment. Error bars represent mean ± SEM (n = 3).

(C) Representative blot showing that proteasomal inhibition with MG132 prevents TDP1 degradation. TDP1$^{-/-}$ MEF cells were transfected with FLAG-TDP1 and 24 h later were treated with CHX for the indicated time points (h) in the presence or absence of proteasomal inhibitor (MG132) and quantified by densitometry and normalized against actin; the remaining TDP1 level was calculated relative to levels before CHX treatment. Error bars represent mean ± SEM (n = 3).

(D) Representative blot showing that R586 dimethylation promotes TDP1 ubiquitylation and blocks UCHL3 interaction. FLAG-tagged TDP1 constructs (WT, R361K, or R586K) and HA-ubiquitin were co-transfected in HCT116 cells in the absence or presence of CPT (5 μM, 3 h). FLAG-TDP1 variants were immunoprecipitated (IP) using anti-FLAG antibody, and the immune complexes were first blotted with the anti-ubiquitin-specific and anti-UCHL3 antibody and then stripped and re-probed with an anti-FLAG antibody to detect TDP1. The slowly migrating ubiquitylated TDP1 (Ub-TDP1) is indicated. Aliquots (10%) of the input show UCHL3 levels before immunoprecipitation.

(E) TDP1 ubiquitylation was quantified by densitometry analysis following normalization to TDP1 and is presented as an average ±SEM (n = 3).

(F) UCHL3 binding with TDP1 variants (WT, R361K, and R586K) were quantified by densitometry analysis following normalization to UCHL3 (input) and is presented as an average ±SEM (n = 3). **p < 0.001, ***p < 0.0001; ns, not significant; p > 0.05; t test.

(G) UCHL3 knockdown rescues ubiquitination in TDP1^{R586K} mutant. FLAG-tagged TDP1 constructs (WT and R586K) were ectopically expressed in UCHL3 knockdown cells. FLAG-TDP1 variants were immunoprecipitated using an anti-FLAG antibody. The immune complexes were blotted with an anti-ubiquitin-specific antibody (representative experiment) and then re-probed with an anti-FLAG antibody to detect TDP1. The slowly migrating ubiquitylated TDP1 (Ub-TDP1) is indicated.

(H) PRMT5 overexpression abrogates UCHL3 interaction with TDP1. GFP-tagged TDP1 alone or co-transfected with FLAG-tagged PRMT5 in HCT116 cells as indicated. GFP-TDP1 was immunoprecipitated using an anti-GFP antibody, and the immune complexes were blotted with an anti-UCHL3 antibody (representative experiment). Aliquots (10%) of the input show FLAG-PRMT5 and UCHL3 levels before immunoprecipitation as detected by anti-FLAG and anti-UCHL3 antibodies, respectively.

mutant TDP1^{R586K}, we detected reduced binding of UCHL3 with TDP1^{WT} or TDP1^{R361K} in the absence of CPT (Figures 3D and 3F), which corresponds to the enrichment of ubiquitylated TDP1 variants (WT and R361K) in the absence of DNA damage (Figures 3D and 3E).

To further examine the UCHL3 dependence on TDP1 arginine methylation, we performed pull-down experiments with FLAG-TDP1 variants (*wild type*; WT, and R586K) in the UCLH3 knockdown cells. We detected a marked increase in the enrichment of ubiquitylated TDP1^{R586K} (Ub-TDP1^{R586K}) in UCLH3 knockdown

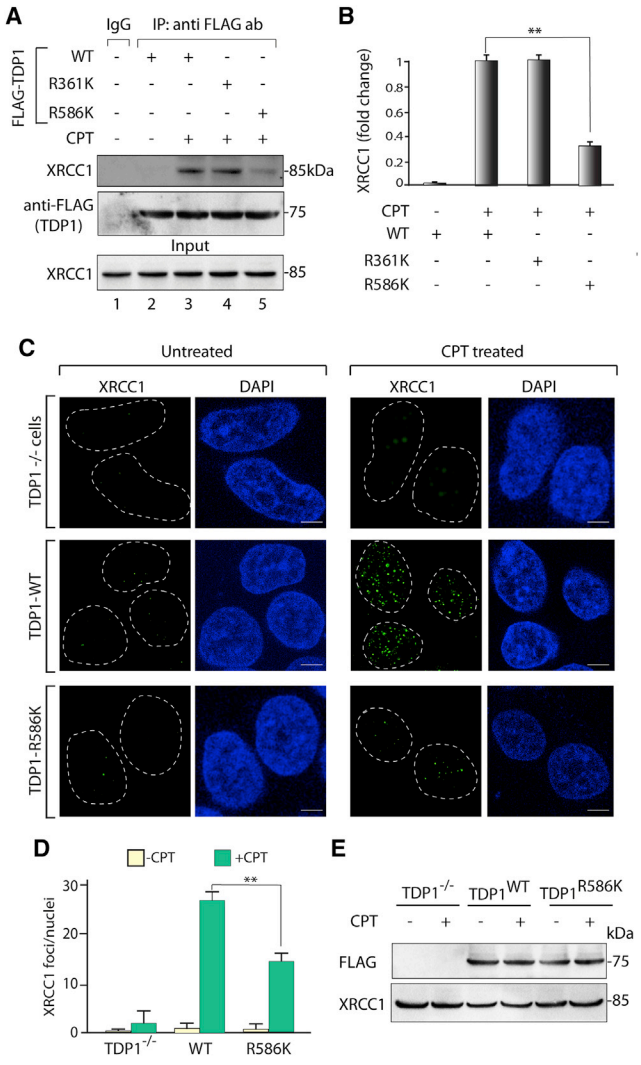

Figure 4. Dimethylation of TDP1 at R586 recruits XRCC1 at Top1cc damage sites

(A and B) R586 dimethylation promotes TDP1 binding to XRCC1. FLAG-tagged TDP1 constructs (WT, R361K, or R586K) were ectopically expressed in HCT116 cells in the absence or presence of CPT (5 μM, 3 h) (A). FLAG-TDP1 variants were immunoprecipitated using anti-FLAG antibody. Immune complexes were blotted with anti-XRCC1-specific antibody and quantified by densitometry (B); Error bars represent mean ± SEM (n = 3). The blot was then stripped and re-probed with an anti-FLAG antibody to show equal loading. Aliquots (10%) of the input show the level of XRCC1 before immunoprecipitation.

(C) CPT-induced XRCC1 foci formation in TDP1$^{-/-}$ MEFs cells expressing FLAG-TDP1^{WT} and FLAG-TDP1^{R586K} or vector control (TDP$^{-/-}$). Representative confocal images of XRCC1 foci formation induced by CPT (5 μM, 3 h). XRCC1 foci are shown in green, and nuclei are stained with DAPI. (Scale bar, 5 μm).

(D) XRCC1 foci per nucleus (marked in dotted circles) was calculated for 20–25 cells using ImageJ software.

(E) Representative western blot showing the equal level of ectopic expression of FLAG-tagged TDP1 variants and endogenous XRCC1 level in TDP1$^{-/-}$ MEFs. *Significant differences: *p < 0.01, **p < 0.001, t test.

cells compared with UCHL3-proficient cells (Figure 3G, Ub-TDP1), consistent with methylation at R586 impeding TDP1-UCHL3 binding independently of DNA damage.

To further test the PRMT5 dependence on the UCHL3-TDP1 binding, we overexpressed FLAG-PRMT5 and co-immunoprecipitated ectopic GFP-TDP1. Figure 3H shows the overexpression of FLAG-PRMT5 in cells markedly abrogating the binding of endogenous UCHL3 with GFP-TDP1. Taking these results together, we conclude that TDP1 arginine methylation at R586 promotes TDP1 ubiquitylation by impeding the association between TDP1 and UCHL3.

TDP1 dimethylation at R586 promotes its association with XRCC1

To investigate the functional role of TDP1 R586 dimethylation *in vivo*, we tested the role of TDP1^{R586K} on its binding with XRCC1. Immunoprecipitation of ectopic FLAG-TDP1^{WT}, FLAG-TDP1^{R361K}, and FLAG-TDP1^{R586K} showed that TDP1^{R586K} was deficient in pulling down XRCC1 from CPT-treated cell extract (Figures 4A and 4B), whereas the binding of XRCC1 with TDP1 was similar for TDP1^{WT} and TDP1^{R361K} (Figures 4A and 4B). Together, these results suggest that R586 dimethylation is critical for the association of TDP1 with XRCC1.

Next, we tested whether TDP1-R586 dimethylation promotes XRCC1 foci formation. Immunofluorescence microscopy was performed in TDP1$^{-/-}$ MEFs cells complemented with either vector control or FLAG-TDP1 variants (WT and R586K). Complementation of *wild-type* TDP1 in TDP1$^{-/-}$ cells facilitates CPT-induced XRCC1 focus formation (Figure 4C), consistent with previous reports (Das et al., 2014). However, complementation of TDP1^{R586K} showed attenuated XRCC1 foci formation after CPT treatment in TDP1$^{-/-}$ cells (Figures 4C and 4D), and this effect was not due to reduced expression of FLAG-TDP1^{R586K} in TDP1$^{-/-}$ cells (Figure 4E), suggesting that R586 dimethylation of TDP1 promotes XRCC1 repair foci formation at Top1cc.

R361 dimethylation enhances the catalytic activity of TDP1

Because TDP1 dimethylation has been implicated in modulating its 3′-phosphodiesterase activity (Rehman et al., 2018), we tested the independent role of TDP1 methylation residues on its catalytic activity by using real-time fluorescence-based assays (Flett et al., 2018). We employed an *ex vivo* approach with immunoprecipitated FLAG-TDP1 variants (WT, R361K, or R586K) as the source of the enzyme (Figure 5A) to test the impact of TDP1 arginine dimethylation on TDP1 catalytic activity (Das et al., 2016; Rehman et al., 2018). FRET-based TDP1 assays were performed using two DNA substrates: an 18-nucleotide single-stranded DNA (ssDNA) (Figure 5B) and a double-stranded DNA hairpin (dsDNA) containing 15 base pairs (Figure 5C). Each substrate had a 5′ fluorophore and a 3′ quencher that ablates fluorescence, as described previously (Flett et al., 2018). Cleavage of the 3′ quencher by TDP1 abolishes FRET, giving rise to fluorescence that can be detected in real time both for the ssDNA and for dsDNA substrates. Figures 5B and 5C show that the 3′ cleavage efficiency of the methylation mutant TDP1 (TDP1^{R361K}) was markedly deficient (~1.5 to 2-fold) compared with its *wild-type* (TDP1^{WT}) or methylation mutant (TDP1^{R586K}) counterpart for both the ssDNA and dsDNA

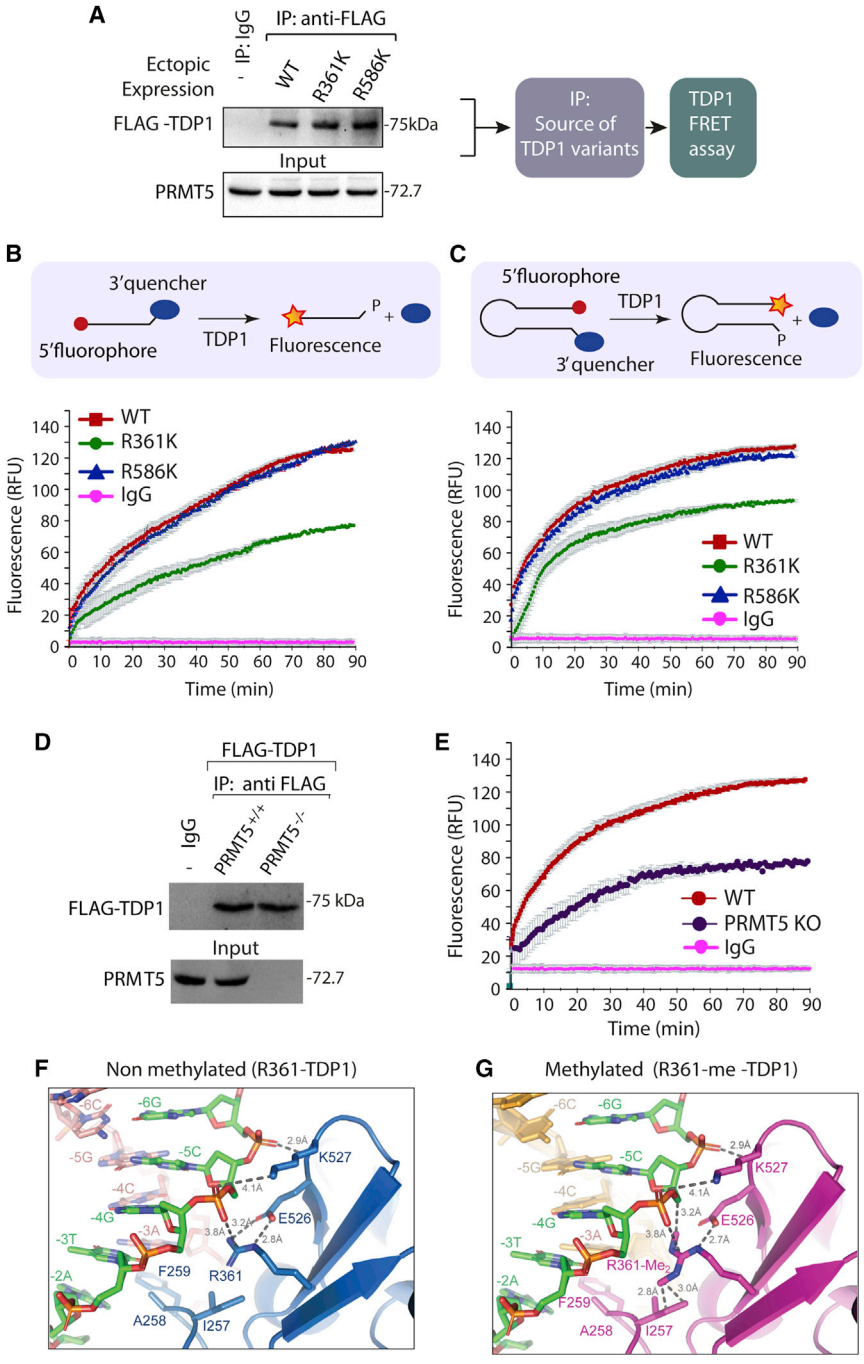

Figure 5. R361 methylation enhances the 3′-phosphodiesterase activity of TDP1

(A) Representative western blot showing equal levels of immunoprecipitated FLAG-tagged TDP1 variants (WT, R361K, or R586K), and the immune complexes were used as the source of TDP1 variants for time-dependent FRET-based TDP1 cleavage assays. Aliquots (10%) of the input show the TDP1 level before immunoprecipitation.

(B and C) FRET-based real-time TDP1 cleavage assays. Schematic representation of activity assays using (B) 18-nt single-stranded fluorescence quencher DNA (ssDNA) substrate and (C) a 15-bp hairpin double-stranded fluorescence quencher DNA (dsDNA). Cleavage of the 3′ quencher (blue ellipse) by TDP1 increases the fluorescence of 5′ fluorophore (red dot). Substrate cleavage by WT, R361K, or R586K TDP1 was measured by fluorescence intensity, in relative fluorescence units (RFU), and plotted as a function of time (min). Error bars represent mean ± SEM (n = 3).

(D) Representative western blot showing equal levels of immunoprecipitated FLAG-tagged TDP1 ectopically expressed in the PRMT5-proficient ($PRMT5^{+/+}$) and PRMT5 knockout ($PRMT5^{-/-}$) cells using anti-FLAG antibody. Aliquots (10%) of the input show the PRMT5 level before immunoprecipitation.

(E) TDP1 cleavage assay of TDP1 immunoprecipitated from $PRMT5^{+/+}$ and $PRMT5^{-/-}$ cells, using dsDNA as substrate, were measured by fluorescence intensity in RFU plotted as a function of time (min). Error bars represent mean ± SEM (n = 3).

(F) Crystal structure of the TDP1(Δ148)-DNA complex, with TDP1 shown as a blue cartoon and relevant side chains as sticks; the scissile DNA strand is pink, and the complementary strand is green. Interactions between TDP1 and the complementary strand are shown as a gray dotted line (distances in Ångstroms).

(G) Structural model of di-methylated R361 TDP1 in complex with duplex DNA; modified TDP1 is purple and the scissile strand is mustard.

substrates. Notably, the cleavage activity by $TDP1^{R586K}$ mutant was similar to the wild-type enzyme ($TDP1^{WT}$) for both the DNA substrates, suggesting that TDP1 dimethylation at R361 promotes its catalytic activity. We further confirmed that the difference in the activities (Figures 5B and 5C) is not due to defects in the DNA-binding abilities of TDP1 variants due to point mutation at the arginine methylation site (R361K) (Figure S3A; see the comparable dissociation constant K_d for $TDP1^{WT}$ and $TDP1^{R361K}$) detected by fluorescence anisotropy experiments (Dexheimer et al., 2010).

To directly test the activities of FLAG-TDP1 purified from *PRMT5 KO* cells, we immunoprecipitated ectopic FLAG-$TDP1^{WT}$ from *PRMT5 KO* cells using anti-FLAG antibody (Figure 5D) and further performed TDP1-mediated fluorescence cleavage assays. Figure 5E shows that TDP1 purified from *PRMT5 KO* cells was enzymatically less active (~2-fold) compared with PRMT5-proficient cells (Figure 5D). Taking these together, we conclude that arginine methylation at R361 promotes the catalytic activity of TDP1.

Modeling the structural impact of TDP1-R361 dimethylation

To explain structurally the increased activity of TDP1 dimethylated at R361 (Figure 5F), we performed simulation-based structural modeling (Figures 5G and S3B). First, we considered the

structural role of R361 in DNA binding by examining the crystal structure of TDP1(Δ148) bound to duplex DNA (Flett et al., 2018). R361 is one of a group of amino acids forming a track of positive surface charge that binds the complementary DNA strand. The R361 guanidium Cz is 3.8 Å from a non-bridging oxygen of the -5C nucleotide (Figure 5F), consistent with an electrostatic protein-DNA interaction. In addition, R361 NHε and NHη1 hydrogen bond with the E526 side-chain carboxyl (Figure 5F). E526 is at the start of a surface-exposed β-turn that changes conformation and becomes more ordered upon duplex DNA binding (Flett et al., 2018). K527 is conserved and forms electrostatic and hydrogen bond interactions with the non-bridging phosphate backbone oxygen of -5C and -6G on the complementary DNA strand via the side-chain $N\zeta H_3^+$ and backbone amide, respectively (Figure 5F). Thus, R361 is central to a network of interactions that contributes to the binding of TDP1(Δ148) to duplex DNA and is likely to be important for catalysis.

Next, we modeled the effect of symmetrical R361 dimethylation, which adds one methyl to each Nη of the guanidinium group, creating a triskelion side-chain structure (Figure 5G). Whereas the electrostatic interaction between the charged dimethylated R361 side chain and the -5C DNA phosphate oxygen is retained, one hydrogen bond, between NHη1 and the E526 carboxyl, is lost. However, three additional hydrophobic interactions compensate for this loss: the Nη1-attached methyl interacts with the C5′ of the -5C ribose on the complementary DNA strand (distance 3.2 Å, Figure 5G), enhancing TDP1's binding to DNA, in contrast to dimethylated R586 (Figure S3B). The Nη2-attached methyl forms hydrophobic contacts with the I257 Cγ and Cδ (2.8 and 3.0 Å, respectively), part of the hydrophobic loop involved in DNA strand separation and DNA processing (Flett et al., 2018). Taken together, these additional interactions form an extended network that directly links the hydrophobic loop, the β-turn, and the DNA binding surface, structural features important for TDP1 catalysis. These unique interactions provide a structural explanation for the increased activity of TDP1 in real-time FRET-based assays (Figures 5B and 5C) upon R361 dimethylation.

Co-operation between R361 and R586 dimethylation protects cells against CPT-induced DNA damage

To dissect the biological significance of TDP1 dimethylation at R361 and R586 sites *in vivo*, we expressed FLAG-tagged TDP1 variants (WT, R361K and R586K) in $TDP1^{-/-}$ cells and investigated the role of R361 and R586 independently in DNA repair using γH2AX, comet, and survival assays.

The γH2AX foci is an established marker for Top1cc-induced DSBs (Das et al., 2009, 2014; Rehman et al., 2018). We analyzed the role of R361 and R586 independently in DNA repair by monitoring CPT-induced γH2AX foci formation and disappearance by using immunofluorescence microscopy. Figures 6A and 6B show that CPT-induced γH2AX foci were markedly higher in $TDP1^{-/-}$ cells complemented with $TDP1^{R361K}$ and $TDP1^{R586K}$ compared with $TDP1^{-/-}$ cells expressing *wild-type* $TDP1^{WT}$. Correspondingly, using comet assays, we detected higher levels of DNA breaks due to defective TDP1 methylation at $TDP1^{R361K}$ or $TDP1^{R586K}$, which were rescued by expressing $TDP1^{WT}$ in $TDP1^{-/-}$ cells (Figure 6C). After washout of CPT, both $TDP1^{R361K}$ and $TDP1^{R586K}$ showed persistent DNA breaks (Figure 6C) and γH2AX foci (Figure 6A; see the quantification 6B) indicating the slow reversal kinetics of Top1cc and defective DNA repair (Figure 6B). Under similar conditions, we also noted that $TDP1^{-/-}$ cells expressing $TDP1^{R361K}$ accumulated increased CPT-induced DNA breaks (Figure 6C) and γH2AX foci (Figure 6B) compared with $TDP1^{R586K}$, which may be attributed to its catalytic activity defects in hydrolyzing Top1cc.

Finally, we tested the impact of the R361K and R586K mutations on cell survival. Survival assays (Figure 6D) were performed with $TDP1^{-/-}$ cells complemented with WT, R361K, and R586K. Figure 6D shows that expression of the wild-type TDP1 protected $TDP1^{-/-}$ cells significantly better than the independent methylation mutant TDP1 (R361K and R586K), which agrees with defective DNA repair activity of $TDP1^{R361K}$ and $TDP1^{R586K}$ in response to CPT-induced DNA damage. Taken together, these results provide evidence that both of the arginine methylation mutants of TDP1 were defective in DNA repair.

DISCUSSION

In the present study, we have uncovered a mechanism by which PRMT5-dependent methylation at residues R361 and R586 controls homeostasis of cellular TDP1 that is critical for maintaining genome stability. Using *PRMT5 KO* cells, we have shown that loss of TDP1 arginine methylation results in compromised TDP1 proteostasis, which leads to the accumulation of enzymatically less active TDP1 protein that failed to rescue cells from CPT-induced cytotoxicity. We have also demonstrated that methylation of TDP1 at R586 promotes ubiquitin/proteasome-dependent TDP1 proteostasis to maintain its steady-state level within cells. Furthermore, compromised TDP1 proteostasis due to defective TDP1-R586 methylation impairs UCHL3-TDP1 binding and accumulates TDP1 in the cells (model). TDP1 methylation promotes XRCC1 repair foci at CPT-induced DNA damage sites. Intriguingly, DNA damage induces R361 dimethylation and enhances the 3′-phosphodiesterase activity of TDP1 for the efficient repair of trapped Top1cc. Our current work offers evidence that both the arginine methylation sites of TDP1 facilitate the DNA repair activity.

Post-translational modifications (PTM) ensure efficient propagation of damage signals for DNA repair and genomic integrity (Bhattacharjee et al., 2022; Katyal et al., 2007; Pommier et al., 2016; Shiloh and Ziv, 2013). Several PTMs are important elements in the regulation of TDP1 recruitment, subcellular distribution, and stability of DNA damage response (El-Khamisy, 2011; Chowdhuri and Das, 2021; Pommier et al., 2014). CPT or ionizing radiation-induced DSBs advocate $TDP1^{S81}$ phosphorylation by ATM and/or DNA-PK that stabilizes TDP1 (Chiang et al., 2010; Das et al., 2009). The half-life of TDP1 is also increased through TDP1 PARylation mediated by PARP1, promoting recruitment of TDP1 with XRCC1 (X-ray cross-complementing group 1) at CPT-induced DNA damage sites (Das et al., 2014). Intriguingly, the ubiquitin-proteasome system plays an important role in regulating TDP1 turnover, which is fine-tuned by the deubiquitylase enzyme UCHL3, controlling TDP1 proteostasis (Liao et al., 2018). PRMT5 catalyzes TDP1 dimethylation at R361 and

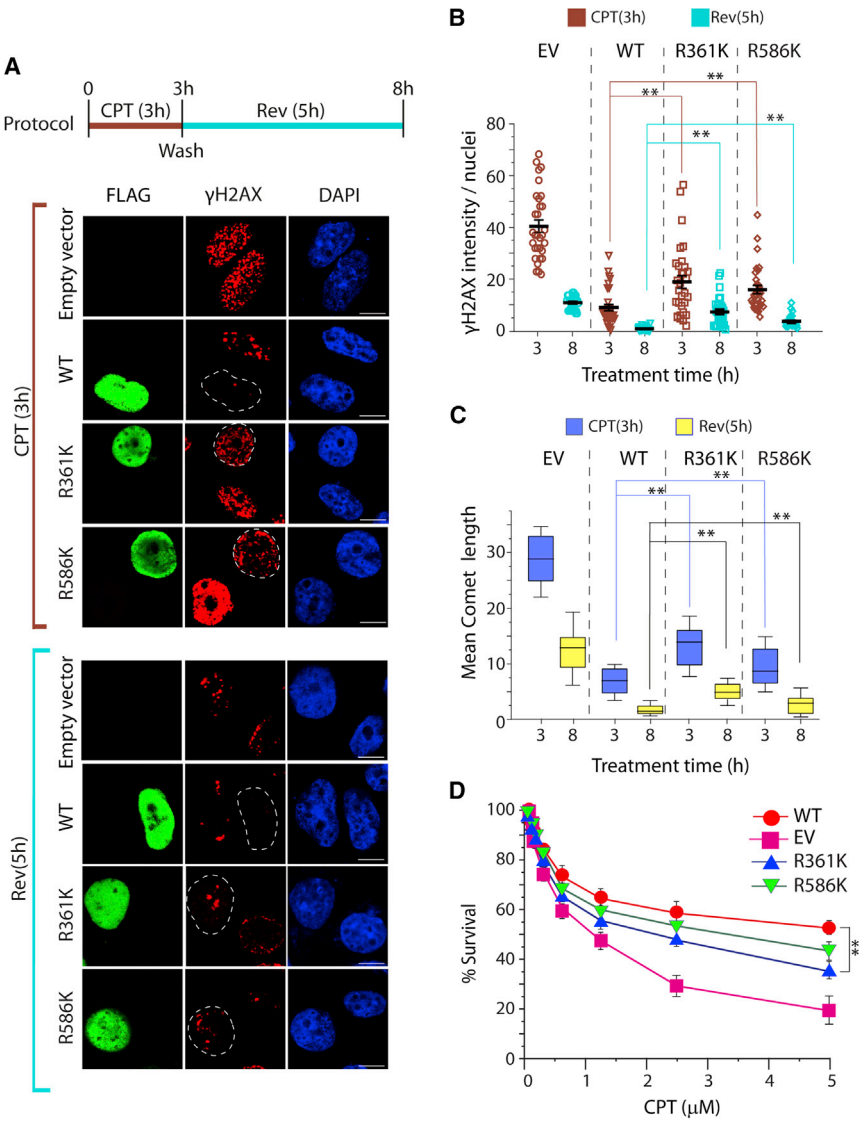

Figure 6. R361 and R586 dimethylation-TDP1 promote cell survival and DNA repair in response to CPT

(A and B) γH2AX kinetics after CPT removal. TDP1$^{-/-}$ MEF cells were transfected with FLAG-TDP1^{WT}, FLAG-TDP1^{R361K}, FLAG-TDP1^{R586K}, or empty vector (EV). Twenty-four hours after transfection, cells were treated with CPT (5 μM, 3 h). After CPT removal (Rev), cells were cultured in a drug-free medium for the indicated times (top). Representative confocal images showing expression of FLAG-TDP1 variants detected by immunofluorescence staining with anti-FLAG antibody (green). γH2AX induction is shown in red. Cells were counterstained with DAPI to visualize nuclei (blue). Nuclei are outlined in dashed white lines expressing ectopic FLAG-TDP1 variants (scale bar, 5 μm).

(B) Quantification of γH2AX intensity per nucleus after CPT removal obtained from immunofluorescence confocal microscopy, calculated for 20–25 cells (mean ± SEM) and plotted as a function of treatment time (h). *Statistically significant difference: **p < 0.001, t test.

(C) Quantification of CPT-induced DNA strand breaks measured by alkaline comet assays in TDP1$^{-/-}$ MEF cells transfected with EV or FLAG-tagged TDP1 constructs (WT, R361K, or R586K) upon CPT treatment (5 μM, 3 h) and CPT removal, as indicated. CPT-induced DNA strand breaks were calculated for 20–25 cells (average ± SEM).

(D) Cell survival curves of TDP1$^{-/-}$ MEF cells transfected with EV or FLAG-tagged TDP1 constructs (WT, R361K, or R586K). CPT-induced cytotoxicity (%) was calculated with respect to the untreated control. Error bars represent SD (n = 3). *Statistically significant differences: **p < 0.001, t test.

R586, which stimulates TDP1's repair function and promotes cell survival in response to CPT and ionizing radiation (Rehman et al., 2018).

More precisely, the arginine methylation mutant TDP1^{R586K} shows an increased half-life in the CHX chase experiments compared with the additional methylation mutant site TDP1^{R361K} (Figures 3A and 3B), implying that R586 methylation regulates TDP1 turnover in the absence of exogenous DNA damage.

Interestingly, we detected that TDP1^{R586K} was markedly deficient in pulling down slower migrating ubiquitylated TDP1 (Ub-TDP1; Figures 3D and S2A), compared with its wild-type or R361K methylation mutant TDP1 (Figure 3E), favoring the interpretation that R586 methylation promotes TDP1 ubiquitylation. Intriguingly, UCHL3 is a DUB that binds with TDP1 to remove conjugated ubiquitin chains, thereby, rescuing TDP1 from degradation (Liao et al., 2018). Remarkably, the association of TDP1^{R586K} with UCHL3 remains unchanged even in the presence of DNA damage with CPT (Figure 3D, UCHL3, and 3F). Therefore, increased binding of UCHL3 with R586K-methylation mutant TDP1 agrees with the decreased binding of ubiquitin with TDP1^{R586K} (Figures 3D and 3E), implying that the interplay between R586 methylation and ubiquitylation promotes TDP1 proteostasis through the ubiquitin-proteasome-mediated pathway (Figure 3C). Additionally, *UCLH3 knockdown* cells show enrichment of ubiquitylated-TDP1^{R586K} (Figure 3G), whereas overexpression of PRMT5 abrogates the binding of TDP1 to UCHL3 (Figure 3H), suggesting that methylation at R586 impedes TDP1-UCHL3 binding independently of DNA damage. Therefore, defective TDP1 arginine methylation at R586 (Figure 1A) accumulates TDP1 in the *PRMT5 KO* cells (Figures 1B and 1C) that abrogates TDP1 proteostasis. Notably, this is consistent with the role of PRMT5-mediated arginine dimethylation of downstream target proteins, like KLF4, E2F1, SREBP1, GLI1, 53BP1, and γH2AX, regulating their turnover, stability, and subcellular localization (Abe et al., 2019; Du et al., 2019; Hu et al., 2015; Hwang et al., 2020; Liu et al., 2016).

Intriguingly, we detected no significant difference between the half-life of TDP1 methylation mutant at R586 or R361 and *wild-type* TDP1 upon DNA damage (Figure 2E, +CPT, and Figure 3B), leading us to conclude that DNA damage stabilizes TDP1

independently of arginine methylation. Therefore, alternatively, we proposed in our model that DNA-damage-induced TDP1 stability is plausibly promoted by TDP1-S81 phosphorylation (Chiang et al., 2010; Das et al., 2009), (Figure 3B). This is further supported by our co-immunoprecipitation experiments, which show that FLAG-TDP1^{KK} enriches TDP1^{S81} phosphorylation ~1.5-fold in the presence of CPT (Figure S4). These data favor our interpretation that CPT-induced DNA damage increases TDP1 stability independently of TDP1-arginine methylation.

XRCC1 is devoid of any enzymatic activity but binds with the repair enzymes, including poly(ADP-ribose) polymerase (PARP), ligase IIIα, pol β and PNKP, and has been primarily implicated in single-strand break rejoining in the BER pathway (Caldecott, 2019; Horton et al., 2017). XRCC1 has previously been found in association with TDP1 and has been implicated in the repair of Top1cc (Das et al., 2014; Chowdhuri and Das, 2021; Pommier et al., 2014), which could be related to its interactions with PARP1, PNKP, and ligase 3 (Caldecott, 2019; Horton et al., 2017). We provide evidence that R586 methylation enhances TDP1 interactions with XRCC1 and the recruitment of XRCC1 foci at Top1cc damage sites (Figure 4). Intriguingly, TDP1-R361 methylation promotes TDP1 enzymatic activity that facilitates Top1cc repair (Figure 5). Therefore, we surmise that R586 methylation of TDP1 stimulates efficient propagation of the DDR signaling through XRCC1 foci recruitment.

The mechanistic implications of TDP1 methylation at R361 seem to involve the modulation of enzymatic activity (Figure 5). As deciphered from the real-time FRET-based fluorescence cleavage assay (Flett et al., 2018), the 3′ cleavage activity of the R361K methylation mutant TDP1 was markedly deficient (~1.5- to 2-fold) compared with its wild-type or R586K methylation mutant TDP1 (Figures 5B and 5C). Arginine side chains can promote protein interactions with DNA: the positively charged guanidinium group interacts electrostatically with negatively charged backbone phosphate oxygens, and five potential hydrogen bond donors can interact with backbone phosphate oxygens or with DNA bases. Although dimethylation of arginine retains the positive charge, and therefore the potential for electrostatic interactions, it replaces two of the hydrogen bond donors with bulkier hydrophobic methyl groups (Guccione and Richard, 2019). TDP1-duplex DNA co-crystal structures showed that a hydrophobic loop separates the complementary and scissile DNA strands, promoting cleavage (Flett et al., 2018). Upon dimethylation of R361, unique hydrophobic interactions are established with the complementary-strand backbone, thus stabilizing the separation of two strands near the active site for an efficient cleavage, consistent with the increased cleavage of 3′-phosphotyrosyl linkages upon TDP1-R361 dimethylation (Figures 5B and 5C).

In conclusion, the present study reveals the significance of TDP1 arginine methylation for the repair of Top1cc. Here, we uncover the crosstalk between TDP1 arginine methylation at R586 and ubiquitylation, a determining factor for the association of TDP1 with UCHL3, thus acting as a switch for regulation of endogenous TDP1 turnover in the absence of exogenous DNA damage.

Limitations of the study

While our findings divulge the role of arginine symmetric dimethylation in regulating TDP1 proteostasis and catalytic activity in proliferating cancer cell lines and MEF cells, it is still unclear whether this phenomenon extends to post-mitotic neuronal cells. Furthermore, it has not been investigated whether loss of PRMT5-mediated TDP1 dimethylation causes the human neurological manifestation associated with SCAN1 disease. Additional studies to identify the specific E3 ubiquitin ligase, the TDP1 ubiquitylation sites, and the crosstalk of ubiquitylation with R586 dimethylation would strengthen our understanding of the interplay between these two post-translational modifications for TDP1 homeostasis.

STAR★METHODS

Detailed methods are provided in the online version of this paper and include the following:

- KEY RESOURCES TABLE
- RESOURCE AVAILABILITY
  - Lead contact
  - Materials availability
  - Data and code availability
- EXPERIMENTAL MODELS AND SUBJECT DETAILS
- METHOD DETAILS
  - Treatment and transfections
  - Expression constructs and CRISPR/Cas9-mediated PRMT5 gene knockout
  - Quantification of nuclear gene transcription by real Time PCR
  - Cell extracts, immunoblotting and immunoprecipitation
  - Immunocytochemistry and confocal microscopy
  - FRET-based TDP1 activity assay
  - Fluorescence anisotropy
  - Structural modeling of TDP1 dimethylation
  - Alkaline COMET assays
  - Cell survival assays
- QUANTIFICATION AND STATISTICAL ANALYSIS

SUPPLEMENTAL INFORMATION

Supplemental information can be found online at https://doi.org/10.1016/j.celrep.2022.110940.

ACKNOWLEDGMENTS

B.B.D.'s team is supported by a DBT India alliance fellowship grant (Award# IA/I/13/1/500888), SERB core research grant (EMR/2017/001652); and an S. Ramachandran National Bioscience Award for Career Development (NBACD)-2019 grant (102/IFD/SAN/3574/2019-20). S. Bhattacharjee is the recipient of a CSIR-NET Senior Research Fellowship respectively, India.

AUTHOR CONTRIBUTIONS

S. Bhattacharjee, I.R., S. Basu., S.N., and J.R. performed the experiments; S. Bhattacharjee, I.R., J.R., and B.B.D. designed experiments, analyzed the data, and wrote the manuscript; B.B.D. provided supervision.

DECLARATION OF INTERESTS

The authors declare no competing interests.

Received: June 8, 2021
Revised: April 5, 2022
Accepted: May 20, 2022
Published: June 14, 2022

REFERENCES

Abe, Y., Suzuki, Y., Kawamura, K., and Tanaka, N. (2019). MEP50/PRMT5-mediated methylation activates GLI1 in Hedgehog signalling through inhibition of ubiquitination by the ITCH/NUMB complex. Commun. Biol. *2*, 1–12. https://doi.org/10.1038/s42003-018-0275-4.

Antony, S., Marchand, C., Stephen, A.G., Thibaut, L., Agama, K.K., Fisher, R.J., and Pommier, Y. (2007). Novel high-throughput electrochemiluminescent assay for identification of human tyrosyl-DNA phosphodiesterase (Tdp1) inhibitors and characterization of furamidine (NSC 305831) as an inhibitor of Tdp1. Nucleic Acids Res. *35*, 4474–4484. https://doi.org/10.1093/nar/gkm463.

Auclair, Y., and Richard, S. (2013). The role of arginine methylation in the DNA damage response. DNA Repair *12*, 459–465. https://doi.org/10.1016/j.dnarep.2013.04.006.

Bedford, M.T., and Clarke, S.G. (2009). Protein arginine methylation in mammals: who, what, and why. Molecular cell *33*, 1–13. https://doi.org/10.1016/j.molcel.2008.12.013.

Bhattacharjee, S., Rehman, I., Nandy, S., and Das, B.B. (2022). Post-translational Regulation of Tyrosyl-DNA Phosphodiesterase (TDP1 and TDP2) for the Repair of the Trapped Topoisomerase-DNA Covalent Complex (DNA Repair), p. 103277.

Caldecott, K.W. (2019). XRCC1 protein; Form and function. DNA Repair *81*, 102664. https://doi.org/10.1016/j.dnarep.2019.102664.

Capranico, G., Marinello, J., and Chillemi, G. (2017). Type i DNA topoisomerases. J. Med. Chem. *60*, 2169–2192. https://doi.org/10.1021/acs.jmedchem.6b00966.

Chiang, S.-C., Carroll, J., and El-Khamisy, S.F. (2010). TDP1 serine 81 promotes interaction with DNA ligase IIIα and facilitates cell survival following DNA damage. Cell Cycle *9*, 588–595. https://doi.org/10.4161/cc.9.3.10598.

Cho, E.C., Zheng, S., Munro, S., Liu, G., Carr, S.M., Moehlenbrink, J., Lu, Y.C., Stimson, L., Khan, O., Konietzny, R., et al. (2012). Arginine methylation controls growth regulation by E2F-1. EMBO J. *31*, 1785–1797. https://doi.org/10.1038/emboj.2012.17.

Chowdhuri, S.P., and Das, B.B. (2021). Top1-PARP1 association and beyond: from DNA topology to break repair. NAR Cancer *3*, zcab003. https://doi.org/10.1093/narcan/zcab003.

Clague, M.J., Urbé, S., and Komander, D. (2019). Breaking the chains: deubiquitylating enzyme specificity begets function. Nat. Rev. Mol. Cell Biol. *20*, 338–352. https://doi.org/10.1038/s41580-019-0099-1.

Das, B.B., Antony, S., Gupta, S., Dexheimer, T.S., Redon, C.E., Garfield, S., Shiloh, Y., and Pommier, Y. (2009). Optimal function of the DNA repair enzyme TDP1 requires its phosphorylation by ATM and/or DNA-PK. Embo j *28*, 3667–3680. https://doi.org/10.1038/emboj.2009.302.

Das, B.B., Dexheimer, T.S., Maddali, K., and Pommier, Y. (2010). Role of tyrosyl-DNA phosphodiesterase (TDP1) in mitochondria. Proc. Natl. Acad. Sci. USA *107*, 19790–19795. https://doi.org/10.1073/pnas.1009814107.

Das, B.B., Ghosh, A., Bhattacharjee, S., and Bhattacharyya, A. (2021). Trapped topoisomerase-DNA covalent complexes in the mitochondria and their role in human diseases. Mitochondrion *60*, 234–244. https://doi.org/10.1016/j.mito.2021.08.017.

Das, B.B., Huang, S.y.N., Murai, J., Rehman, I., Amé, J.C., Sengupta, S., Das, S.K., Majumdar, P., Zhang, H., Biard, D., et al. (2014). PARP1-TDP1 coupling for the repair of topoisomerase I-induced DNA damage. Nucleic Acids Res. *42*, 4435–4449. https://doi.org/10.1093/nar/gku088.

Das, S.K., Rehman, I., Ghosh, A., Sengupta, S., Majumdar, P., Jana, B., and Das, B.B. (2016). Poly (ADP-ribose) polymers regulate DNA topoisomerase I (Top1) nuclear dynamics and camptothecin sensitivity in living cells. Nucleic Acids Res. *44*, 8363–8375. https://doi.org/10.1093/nar/gkw665.

Dexheimer, T.S., Stephen, A.G., Fivash, M.J., Fisher, R.J., and Pommier, Y. (2010). The DNA binding and 3′-end preferential activity of human tyrosyl-DNA phosphodiesterase. Nucleic Acids Res. *38*, 2444–2452. https://doi.org/10.1093/nar/gkp1206.

Du, C., Hansen, L.J., Singh, S.X., Wang, F., Sun, R., Moure, C.J., Roso, K., Greer, P.K., Yan, H., and He, Y. (2019). A PRMT5-RNF168-SMURF2 Axis controls H2AX proteostasis. Cell Rep. *28*, 3199–3211.e5, e3195. https://doi.org/10.1016/j.celrep.2019.08.031.

Duffy, S., Fam, H.K., Wang, Y.K., Styles, E.B., Kim, J.-H., Ang, J.S., Singh, T., Larionov, V., Shah, S.P., Andrews, B., et al. (2016). Overexpression screens identify conserved dosage chromosome instability genes in yeast and human cancer. Proc. Natl. Acad. Sci. USA *113*, 9967–9976. https://doi.org/10.1073/pnas.1611839113.

El-Khamisy, S.F. (2011). To live or to die: a matter of processing damaged DNA termini in neurons. EMBO Mol. Med. *3*, 78–88. https://doi.org/10.1002/emmm.201000114.

Emsley, P., Lohkamp, B., Scott, W.G., and Cowtan, K. (2010). Features and development of coot. Acta Crystallogr. Sect. D Biol. Crystallogr. *66*, 486–501. https://doi.org/10.1107/S0907444910007493.

Flett, F.J., Ruksenaite, E., Armstrong, L.A., Bharati, S., Carloni, R., Morris, E.R., Mackay, C.L., Interthal, H., and Richardson, J.M. (2018). Structural basis for DNA 3′-end processing by human tyrosyl-DNA phosphodiesterase 1. Nat. Commun. *9*, 1–13. https://doi.org/10.1038/s41467-017-02530-z.

Ghosh, A., Bhattacharjee, S., Chowdhuri, S.P., Mallick, A., Rehman, I., Basu, S., and Das, B.B. (2019). SCAN1-TDP1 trapping on mitochondrial DNA promotes mitochondrial dysfunction and mitophagy. Sci. Adv. *5*, eaax9778. https://doi.org/10.1126/sciadv.aax9778.

Groen, E.J.N., and Gillingwater, T.H. (2015). UBA1: at the crossroads of ubiquitin homeostasis and neurodegeneration. Trends Mol. Med. *21*, 622–632. https://doi.org/10.1016/j.molmed.2015.08.003.

Guccione, E., and Richard, S. (2019). The regulation, functions and clinical relevance of arginine methylation. Nat. Rev. Mol. Cell Biol. *20*, 642–657. https://doi.org/10.1038/s41580-019-0155-x.

Guo, Z., Zheng, L., Xu, H., Dai, H., Zhou, M., Pascua, M.R., Chen, Q.M., and Shen, B. (2010). Methylation of FEN1 suppresses nearby phosphorylation and facilitates PCNA binding. Nat. Chem. Biol. *6*, 766–773. https://doi.org/10.1038/nchembio.422.

He, W., Ma, X., Yang, X., Zhao, Y., Qiu, J., and Hang, H. (2011). A role for the arginine methylation of Rad9 in checkpoint control and cellular sensitivity to DNA damage. Nucleic Acids Res. *39*, 4719–4727. https://doi.org/10.1093/nar/gkq1264.

Hipp, M.S., Kasturi, P., and Hartl, F.U. (2019). The proteostasis network and its decline in ageing. Nat. Rev. Mol. Cell Biol. *20*, 421–435. https://doi.org/10.1038/s41580-019-0101-y.

Hirano, R., Interthal, H., Huang, C., Nakamura, T., Deguchi, K., Choi, K., Bhattacharjee, M.B., Arimura, K., Umehara, F., Izumo, S., et al. (2007). Spinocerebellar ataxia with axonal neuropathy: consequence of a Tdp1 recessive neomorphic mutation? EMBO J. *26*, 4732–4743. https://doi.org/10.1038/sj.emboj.7601885.

Horton, J.K., Stefanick, D.F., Zhao, M.-L., Janoshazi, A.K., Gassman, N.R., Seddon, H.J., and Wilson, S.H. (2017). XRCC1-mediated repair of strand breaks independent of PNKP binding. DNA Repair *60*, 52–63. https://doi.org/10.1016/j.dnarep.2017.10.007.

Hu, D., Gur, M., Zhou, Z., Gamper, A., Hung, M.-C., Fujita, N., Lan, L., Bahar, I., and Wan, Y. (2015). Interplay between arginine methylation and ubiquitylation regulates KLF4-mediated genome stability and carcinogenesis. Nat. Commun. *6*, 1–15. https://doi.org/10.1038/ncomms9419.

Hudson, J.J., Chiang, S.-C., Wells, O.S., Rookyard, C., and El-Khamisy, S.F. (2012). SUMO modification of the neuroprotective protein TDP1 facilitates chromosomal single-strand break repair. Nat. Commun. *3*, 1–13. https://doi.org/10.1038/ncomms1739.

Hwang, J.W., Kim, S.-N., Myung, N., Song, D., Han, G., Bae, G.-U., Bedford, M.T., and Kim, Y.K. (2020). PRMT5 promotes DNA repair through methylation

of 53BP1 and is regulated by Src-mediated phosphorylation. Commun. Biol. *3*, 1–13. https://doi.org/10.1038/s42003-020-01157-z.

Interthal, H., Chen, H.J., and Champoux, J.J. (2005). Human Tdp1 cleaves a broad spectrum of substrates, including phosphoamide linkages. J. Biol. Chem. *280*, 36518–36528. https://doi.org/10.1074/jbc.M508898200.

Jansson, M., Durant, S.T., Cho, E.-C., Sheahan, S., Edelmann, M., Kessler, B., and La Thangue, N.B. (2008). Arginine methylation regulates the p53 response. Nat. Cell Biol. *10*, 1431–1439. https://doi.org/10.1038/ncb1802.

Karkhanis, V., Hu, Y.-J., Baiocchi, R.A., Imbalzano, A.N., and Sif, S. (2011). Versatility of PRMT5-induced methylation in growth control and development. Trend in Biochemical Sciences *36*, 633–641. https://doi.org/10.1016/j.tibs.2011.09.001.

Katyal, S., El-Khamisy, S.F., Russell, H.R., Li, Y., Ju, L., Caldecott, K.W., and McKinnon, P.J. (2007). TDP1 facilitates chromosomal single-strand break repair in neurons and is neuroprotective in vivo. EMBO J. *26*, 4720–4731. https://doi.org/10.1038/sj.emboj.7601869.

Kawale, A.S., and Povirk, L.F. (2018). Tyrosyl-DNA phosphodiesterases: rescuing the genome from the risks of relaxation. Nucleic Acids Res. *46*, 520–537. https://doi.org/10.1093/nar/gkx1219.

Labbadia, J., and Morimoto, R.I. (2015). The biology of proteostasis in aging and disease. Annu. Rev. Biochem. *84*, 435–464. https://doi.org/10.1146/annurev-biochem-060614-033955.

Liao, C., Beveridge, R., Hudson, J.J., Parker, J.D., Chiang, S.-C., Ray, S., Ashour, M.E., Sudbery, I., Dickman, M.J., and El-Khamisy, S.F. (2018). UCHL3 regulates topoisomerase-induced chromosomal break repair by controlling TDP1 proteostasis. Cell Rep. *23*, 3352–3365. https://doi.org/10.1016/j.celrep.2018.05.033.

Liu, L., Zhao, X., Zhao, L., Li, J., Yang, H., Zhu, Z., Liu, J., and Huang, G. (2016). Arginine methylation of SREBP1a via PRMT5 promotes de novo lipogenesis and tumor growth. Cancer Res. *76*, 1260–1272. https://doi.org/10.1158/0008-5472.CAN-15-1766.

Murai, J., Huang, S.y.N., Das, B.B., Dexheimer, T.S., Takeda, S., and Pommier, Y. (2012). Tyrosyl-DNA phosphodiesterase 1 (TDP1) repairs DNA damage induced by topoisomerases I and II and base alkylation in vertebrate cells. J. Biol. Chem. *287*, 12848–12857. https://doi.org/10.1074/jbc.M111.333963.

Naito, Y., Hino, K., Bono, H., and Ui-Tei, K. (2015). CRISPRdirect: software for designing CRISPR/Cas guide RNA with reduced off-target sites. Bioinformatics *31*, 1120–1123. https://doi.org/10.1093/bioinformatics/btu743.

Pommier, Y. (2006). Topoisomerase I inhibitors: camptothecins and beyond. Nat. Rev. Cancer *6*, 789–802. https://doi.org/10.1038/nrc1977.

Pommier, Y., Huang, S.y.N., Gao, R., Das, B.B., Murai, J., and Marchand, C. (2014). Tyrosyl-DNA-phosphodiesterases (tdp1 and tdp2). DNA Repair *19*, 114–129. https://doi.org/10.1016/j.dnarep.2014.03.020.

Pommier, Y., Sun, Y., Huang, S.y.N., and Nitiss, J.L. (2016). Roles of eukaryotic topoisomerases in transcription, replication and genomic stability. Nat. Rev. Mol. Cell Biol. *17*, 703–721. https://doi.org/10.1038/nrm.2016.111.

Popovic, D., Vucic, D., and Dikic, I. (2014). Ubiquitination in disease pathogenesis and treatment. Nat. Med. *20*, 1242–1253. https://doi.org/10.1038/nm.3739.

Ravid, T., and Hochstrasser, M. (2008). Diversity of degradation signals in the ubiquitin-proteasome system. Nat. Rev. Mol. Cell Biol. *9*, 679–689. https://doi.org/10.1038/nrm2468.

Rehman, I., Basu, S.M., Das, S.K., Bhattacharjee, S., Ghosh, A., Pommier, Y., and Das, B.B. (2018). PRMT5-mediated arginine methylation of TDP1 for the repair of topoisomerase I covalent complexes. Nucleic Acids Res. *46*, 5601–5617. https://doi.org/10.1093/nar/gky291.

Shiloh, Y., and Ziv, Y. (2013). The ATM protein kinase: regulating the cellular response to genotoxic stress, and more. Nat. Rev. Mol. Cell Biol. *14*, 197–210. https://doi.org/10.1038/nrm3546.

Sordet, O., Redon, C.E., Guirouilh-Barbat, J., Smith, S., Solier, S., Douarre, C., Conti, C., Nakamura, A.J., Das, B.B., Nicolas, E., et al. (2009). Ataxia telangiectasia mutated activation by transcription- and topoisomerase I-induced DNA double-strand breaks. EMBO Rep. *10*, 887–893. https://doi.org/10.1038/embor.2009.97.

Swatek, K.N., and Komander, D. (2016). Ubiquitin modifications. Cell Res. *26*, 399–422. https://doi.org/10.1038/cr.2016.39.

Takashima, H., Boerkoel, C.F., John, J., Saifi, G.M., Salih, M.A., Armstrong, D., Mao, Y., Quiocho, F.A., Roa, B.B., Nakagawa, M., et al. (2002). Mutation of TDP1, encoding a topoisomerase I-dependent DNA damage repair enzyme, in spinocerebellar ataxia with axonal neuropathy. Nat. Genet. *32*, 267–272. https://doi.org/10.1038/ng987.

Yang, S.-w., Burgin, A.B., Huizenga, B.N., Robertson, C.A., Yao, K.C., and Nash, H.A. (1996). A eukaryotic enzyme that can disjoin dead-end covalent complexes between DNA and type I topoisomerases. Proc. Natl. Acad. Sci. USA *93*, 11534–11539. https://doi.org/10.1073/pnas.93.21.11534.

Yang, Y., and Bedford, M.T. (2013). Protein arginine methyltransferases and cancer. Nat. Rev. Cancer *13*, 37–50. https://doi.org/10.1038/nrc3409.

Zaksauskaite, R., Thomas, R.C., van Eeden, F., and El-Khamisy, S.F. (2021). Tdp1 protects from topoisomerase 1–mediated chromosomal breaks in adult zebrafish but is dispensable during larval development. Sci. Adv. *7*, eabc4165. https://doi.org/10.1126/sciadv.abc4165.

STAR★METHODS

KEY RESOURCES TABLE

REAGENT or RESOURCE	SOURCE	IDENTIFIER
Antibodies		
Rabbit Polyclonal Anti-dimethyl-Arginine Antibody, symmetric (SYM11)	Millipore	Cat# 07-413; RRID: AB_310595
Rabbit Anti-PRMT5 Polyclonal Antibody	Millipore	Cat# 07-405; RRID: AB_310589
Mouse monoclonal anti-phospho-Histone H2A.X (Ser139) Antibody, clone JBW301	Millipore	Cat# 05-636; RRID: AB_309864
Rabbit Anti-TDP1 Polyclonal Antibody	Abcam	Cat# Ab4166; RRID: AB_304337
Rabbit polyclonal Anti-UCHL3 Antibody	Abcam	Cat# Ab126703; RRID: AB_11129956
Mouse monoclonal Anti- XRCC1 Antibody	Abcam	Cat# Ab1838; RRID: AB_302636
Mouse monoclonal anti-FLAG Antibody (M2)	Sigma-Aldrich	Cat# F3165; RRID: AB_259529
Rabbit polyclonal anti-FLAG Antibody	Sigma-Aldrich	Cat# F7425; RRID: AB_439687
Rabbit polyclonal anti-Ubiquitin Antibody	Santa Cruz Biotechnology	Cat# SC9133; RRID: AB_2180553
Mouse Anti-Actin Monoclonal, Unconjugated, Clone actn05 (c4) antibody	Novus	Cat# NB 600-535; RRID: AB_521546
Rabbit polyclonal anti-GFP antibody	Thermo Fisher Scientific	Cat# A-11122; RRID: AB_221569
Rabbit phospho serine 81-TDP1 (pS81-TDP1)	Das et al., 2009	N/A
Goat anti-Rabbit IgG (H+L) Secondary Antibody, HRP	Thermo Fisher Scientific	Cat# 31460, RRID:AB_228341
Goat Anti-Mouse Mouse IgG-h&l Polyclonal, HRP Conjugated antibody	Novus	Cat# NB 7539, RRID:AB_524788
Goat anti-Mouse IgG (H+L) Secondary Antibody, Alexa Fluor 488-10 nm colloidal gold	Thermo Fisher Scientific	Cat# A-31561, RRID:AB_2536175
Goat Anti-Rabbit IgG (H+L) Highly Cross-adsorbed Antibody, Alexa Fluor 568 Conjugated	Thermo Fisher Scientific	Cat# A-11036, RRID:AB_10563566
Goat anti-Mouse IgG (H+L) Cross-Adsorbed Secondary Antibody, Alexa Fluor 488	Thermo Fisher Scientific	Cat# A-11001, RRID:AB_2534069
Goat anti-Mouse IgG (H+L) Cross-Adsorbed Secondary Antibody, Alexa Fluor 568	Thermo Fisher Scientific	Cat# A-11004, RRID:AB_2534072
Bacterial and virus strains		
E.coli BL21 DE3	Thermo Fisher Scientific	Cat# EC0114
E.coli DH5α	Thermo Fisher Scientific	Cat# 18265017
Chemicals, peptides, and recombinant proteins		
Camptothecin (CPT)	Sigma-Aldrich	Cat# CDS008734
Cycloheximide	Sigma-Aldrich	Cat# 239764
MG-132	Sigma-Aldrich	Cat# 474787
Trizol reagent	Thermo Fisher Scientific	Cat# 15596018
ProLong™ Gold AntifadeMountant with DAPI	Thermo Fisher Scientific	Cat# P36935
Lipofectamine 2000	Thermo Fisher Scientific	Cat# 11668019
X-tremeGENE™ HP DNA Transfection Reagent	Sigma-Aldrich	Cat# 6366244001
DNase	Sigma-Aldrich	Cat# AMPD1
Tris-HCl	Merck-Millipore	Cat# 648310
NaCl	Himedia	Cat# MB023
Sodium Lauryl Sulphateextrapure AR, ACS, 99%	SRL	Cat# 54468
NP-40	Sigma-Aldrich	Cat# I8896
Albumin Bovine (pH 6-7) fraction V for molecular biology (Bovine Serum Albumin, BSA), 98%	SRL	Cat# 85171
Sodium deoxycholate	Sigma-Aldrich	Cat# D6750

(*Continued on next page*)

Continued

REAGENT or RESOURCE	SOURCE	IDENTIFIER
Phosphatase inhibitor	Sigma-Aldrich	Cat# 524636
Dithiotheriotol (DTT)	Sigma-Aldrich	Cat#11583786001
Magnesium Chloride	SRL	Cat# 69396
Protein A/G beads	Santa Cruz	Cat# sc-2003
Glycine	Himedia	Cat# MB013
Paraformaldehyde	Sigma-Aldrich	Cat# P6148
Potassium Chloride extrapure AR, 99.5%	SRL	Cat# 1649161
EDTA	SRL	Cat# 43272
DMSO	Amresco	Cat# 0231
DMEM - Dulbecco's Modified Eagle Medium	ThermoFisher Scientific	Cat# 10569044
Fetal Bovine Serum	Gibco (By Life Technologies)	Cat# 10270106
Trypsin-EDTA (0.05%)	Sigma-Aldrich	Cat# 25300054
cOmplete Mini, EDTA-free (protease inhibitor cocktail)	Sigma-Aldrich	Cat# 4693159001
Proteinase K	Sigma-Aldrich	Cat# P2308
Critical commercial assays		
Reverse transcription kit	Applied Biosystems	Cat# 4368814
QuikChange II XL site-directed mutagenesis kit	Agilent Technologies	Cat# 200521
Deposited Data		
Raw Imaging day	This paper; Mandeley data	https://doi.org/10.17632/wpnpxn9brh.1
Experimental models: Cell lines		
TDP1$^{-/-}$ MEFs	Dr Cornelius F Boerkoel (Centre for Molecular Medicine and Therapeutics, University of British Columbia, Vancouver, British Columbia, Canada)	N/A
HCT116	Developmental Therapeutics Program (NCI, NIH)	N/A
HEK293	ATCC	Cat# CRL-1573
HCT116- *PRMT5 KO*	This Paper	N/A
Oligonucleotides		
Prmt5 gRNA CCTGAATTGCGTCCCCGAAATAG	This paper	N/A
UCHL3 siRNA GAUACCUGGAGAACUAUGA	Genx	M_001270952
Primers for Human TDP1 (Forward: GACGTG GACTGGCTCGTAAA Reverse: GAGCCTTAGCCTCTCTCGCTTATC)	This paper	N/A
Primers for Human Actin (ForwardGACCCAGA TCATGTTTGAGACC Reverse: CATCACGATGCCAGTGGTAC)	(Ghosh et al., 2019)	N/A
Fluorescence based *ex vivo* assay- ssDNA (HEI40) 56-FAM/AGA GGA TCT AAA AGA CTT/3BHQ	(Flett et al., 2018)	N/A
Fluorescence based *ex vivo* assay- dsDNA (HEI50) 56-FAM/AAG TCT TTT AGA TCC CTC CGG ATC TAA AAG ACT T/3BHQ	(Flett et al., 2018)	N/A
Fluorescence anisotropy (HEI41-3P) 56-FAM/AGA GGA TCT AAA AGA CTT-3P	(Dexheimer et al., 2010)	N/A
Fluorescence anisotropy (HEI41-3C) 5' AAGTCTTTTAGATCCTCT 3'	This paper	N/A
Recombinant DNA		
pSpCas9(BB)-2A-GFP (PX458)	Addgene	Cat#48138
pCMV-Tag2B-TDP1 WT (FLAGTDP1^{WT})	(Das et al., 2009)	N/A

(*Continued on next page*)

Continued

REAGENT or RESOURCE	SOURCE	IDENTIFIER
pCMV-Tag2B-TDP1 R361K (FLAGTDP1^{R361K})	(Rehman et al., 2018)	N/A
pCMV-Tag2B-TDP1 R586K (FLAGTDP1^{R586K})	(Rehman et al., 2018)	N/A
pCMV-Tag2B-TDP1 R361K R586K (FLAGTDP1^{KK})	(Rehman et al., 2018)	N/A
pCMV-Tag2B-TDP1R361F R586F (FLAGTDP1^{FF})	This paper	N/A
pEGFP-N2-TDP1 WT (GFP TDP1^{WT})	Gift from Dr. Fritz Boege	N/A
pET15b-His-TDP1 WT (HisTDP1^{WT})	(Antony et al., 2007)	N/A
pET15b-His-TDP1 WT (HisTDP1^{R361K})	This paper	N/A
Software and algorithms		
ImageJ	ImageJ	https://imagej.nih.gov/ij/, RRID:SCR_003070
LAS AF	Leica	https://www.leica-microsystems.com/products/microscope-software/p/leica-las-x-ls/ RRID:SCR_013673
Origin	Origin	http://www.originlab.com/index.aspx?go=PRODUCTS/OriginRRID:SCR_014212
Graphpad Prism	GraphPad Software, Inc	https://www.graphpad.com:443/, RRID:SCR_002798

RESOURCE AVAILABILITY

Lead contact

Further information and requests for resources and reagents should be directed to and will be fulfilled by the lead contact, Benu Brata Das (pcbbd@iacs.res.in).

Materials availability

This study did not generate new unique reagents.

Data and code availability

Original western blot images have been deposited at Mendeley Data and are publicly available as of the date of publication. The DOI is listed in the key resources table. Microscopy data reported in this paper will be shared by the lead contact upon request. Any additional information required to reanalyze the data reported in this paper is available from the lead contact upon request.

EXPERIMENTAL MODELS AND SUBJECT DETAILS

The human colon carcinoma cell line (HCT116) was obtained from the Developmental Therapeutics Program (NCI, NIH). TDP1$^{-/-}$ MEF cells were a kind gift from Dr. Cornelius F Boerkoel (University of British Columbia, Vancouver, British Columbia, Canada). HCT116, HEK293 and TDP1$^{-/-}$primary MEFs cells were grown in Dulbecco's modified Eagle's medium (DMEM) containing 10% fetal calf serum (Life Technologies, Rockville, MD, USA) at 37°C and 5% CO_2.

METHOD DETAILS

Treatment and transfections

Cells were treated with the indicated concentrations of CPT and CHX for the indicated time. Cells were transfected with plasmid DNA using Lipofectamine 2000 (Invitrogen) or X-tremeGENE HP DNA transfection reagent (Roche) according to the manufacturer's protocol. All experiments were performed after 48hrs of transfection (Das et al., 2009, 2010, 2014, 2016). SiRNA transfection were performed as described previously. Cells were transfected with control siRNA or siUCHL3 using Lipofectamine 2000 and transfection was repeated after 48 h, then kept for 24 h before proceeding for immunoprecipitation.

Expression constructs and CRISPR/Cas9-mediated PRMT5 gene knockout

Human FLAG-tagged full-length TDP1 (FLAG-TDP1^{WT}), GFP-tagged TDP1 (GFP-TDP1^{WT}) and His-tagged TDP1 constructs were described previously (Das et al., 2009, 2010, 2014, 2016; Rehman et al., 2018). The TDP1 point mutations R361K, R586K and R361K R586K (KK) were described previously (Rehman et al., 2018). FLAG-tagged R361F R586F (FF) and His-tagged TDP1 R361K were generated using 'QuickChange' protocol (Stratagene, La Jolla, CA, USA). PCR-generated constructs were confirmed by DNA sequencing. For CRISPR-based PRMT5 gene knockout, we used guide (g)RNA sequence 5' CCTGAATTGCGTCCCCGAAATAG 3' against exon 1,

designed and synthesized using CRISPR direct software (Naito et al., 2015). The gRNA was cloned into the pSpCas9(BB)-2A-GFP (PX458), a kind gift from Dr. Debabrata Biswas (CSIR-IICB, India). HCT116 were transfected with gRNA^{PRMT5}, using lipofectamine 2000, to derive clonal cell populations. Using the GFP tag, the transfected cells were sorted with a FACS Aria III Cell Sorter. The monoclonal selection was done on a 96-well plate. Western blot showed that the expression of PRMT5 protein was abolished in selected cell clones.

Quantification of nuclear gene transcription by real Time PCR

Trizol reagent (15596018, Invitrogen) was used to extract the total RNA from indicated cells (1 x 10^6) as per the manufacturer's protocols, which includes the addition of DNase (AMPD1; Sigma) to each sample. Reverse transcription kit (4368814, Applied Biosystems) was utilized to reverse transcribe an aliquot of 1 μg RNA. Real-time PCR was performed on ABI 7500 Thermocycler (A25742, Applied Biosystems). Reaction mixtures comprised 5 μL of 2 x SYBR-Green PCR master mix, 2 μL of reverse transcriptase-produced cDNA diluted 10-fold in a final volume of 10 μL including primers at 25 nM (Table S1). The thermocycling parameters were 95°C for 5 min, 40 cycles at 95°C for 50 s, 50°C (variable) for 50 s, and 72°C for 60 s. Relative gene expression was denominated as a ratio of the gene of interest's expression level to that of RNA of β-actin, assuming values in wild-type cells to be 100%.

Cell extracts, immunoblotting and immunoprecipitation

The whole-cell extracts, immunoprecipitation, and immunoblotting were done following standard protocols as described previously (Das et al., 2009, 2010, 2014, 2016; Rehman et al., 2018). Briefly, cells were lysed in a lysis buffer (10 mM Tris–HCl (pH 8), 150 mM NaCl, 2% SDS, 1% NP40, 0.5% Na-deoxycholate containing complete protease inhibitors) (Roche Diagnostics, Indianapolis, IN) and phosphatase inhibitors (Phosphatase Inhibitor Cocktail, Sigma) under denaturing condition and incubated at 4°C for 2 h. Lysates were centrifuged at 12,000 g at 4°C for 20 min. Supernatants were collected, aliquoted, and stored at −80°C. For immunoprecipitation, cells were lysed in a lysis buffer (50 mM Tris–HCl (pH 7.4), 300 mM NaCl, 0.4% NP40, 10 mM $MgCl_2$, 0.5 mM dithiothreitol supplemented with protease and phosphatase inhibitors), then centrifuged at 15,000 g at 4°C for 20 min and supernatant collected. About 50 μL of protein A/G-PLUS agarose beads (Santa Cruz, CA, USA) were incubated overnight with 5 mg of precleared lysate and indicated antibodies (2–5 μg/mL) at 4°C. The immunocomplexes were isolated by centrifugation, recovered and washed thrice with lysis buffer and subjected to immunoblotting. Gel electrophoresis on 10% Tris-glycine gels and immunoblot analysis were done following standard procedures. Immunoreactivity was detected using ECL chemiluminescence reaction (Amersham) in ChemiDoc™ MP System (Bio-Rad, USA) and densitometric analyses of immunoblots was performed with ImageJ software.

Immunocytochemistry and confocal microscopy

Immunocytochemistry and fluorescence microscopy using a confocal microscope were performed as described previously (Das et al., 2009, 2010, 2014, 2016; Ghosh et al., 2019; Rehman et al., 2018). Briefly, cells were grown on chamber slides (Thermo Scientific™ Nunc™ Lab-Tek™ II Chamber slides), treated with CPT for the indicated time, then fixed for 10 min with 4% paraformaldehyde at room temperature. Anti-rabbit or anti-mouse IgG secondary antibodies labeled with Alexa 488/568 (Invitrogen) were used to detect primary antibodies against XRCC1, FLAG, and γH2AX. 4',6-diamidino-2-phenylindole (DAPI) anti-fade solution (Vector Laboratories, Burlingame, CA, USA) was used to mount the cells. Microscopy was done on Leica TCS SP8 confocal laser-scanning microscope (Germany) with a 63×/1.4 NA oil objective. Leica software was used for image processing which was later sized in Adobe Photoshop 7.0. The γH2AX intensity per nucleus was measured by the fluorescence intensities normalized to the number of cell counts in Adobe Photoshop 7.0.

FRET-based TDP1 activity assay

Fluorescence-based TDP1 activity assay was done as described previously (Flett et al., 2018). FLAG-tagged TDP1 variants (Wild type, R361K, R586K) were immunoprecipitated (IP) with anti-FLAG ab from wildtype or PRMT5-knockout cells and the immune complexes were used as the source of TDP1 variants for the time course cleavage experiments. The ssDNA (HEI40) and dsDNA (HEI50) with 5′ 5(6)-carboxyfluorescein (56-FAM) and 3′ Black Hole Quencher (3BHQ) modification (Table S1) was used as DNA substrate. Briefly, the DNA substrates were dissolved in 10 mM Tris pH 8.0 and 50 mM NaCl. To promote the hairpin formation and to prevent the formation of dimers, HEI50 was heated to 80 °C for 10 min and snap-cooled rapidly on ice. TDP1 immune complexes were incubated with 50 nM and 35 nM DNA substrates respectively for 90 min at 25 °C in 96-well black opaque plates on a SpectraMax M5 multimode microplate reader (Molecular Devices). The reaction buffer contained 100 mM KCl, 10 mM Tris pH 7.5, 1 mM EDTA, 1 mM DTT, 100 μg BSA. The excitation and emission wavelength of the fluorophore were 488 nm and 523 nm respectively. The data were measured using SoftMaxPro software, processed in Microsoft Excel and graphs plotted in GraphPad Prism.

Fluorescence anisotropy

Fluorescence anisotropy titration was done to assess the binding of recombinant TDP1 with DNA as described previously (Dexheimer et al., 2010). Briefly, the fluorescence anisotropy substrates were mixed in an annealing buffer, heated to 95 °C for 10 min then slowly cooled in room temperature to promote annealing. The anisotropy experiments were carried out on a Fluoromax-4 fluorimeter (Horiba) in anisotropy binding buffer (50 mM Tris– HCl (pH 7.5), 25 mM KCl and 2 mM EDTA) in a final volume 200μL. 10 nM of 5'-6 fluorescein 3'phosphate was titrated using varying concentrations of recombinant His-tagged TDP1 WT and R361K protein. The excitation and emission were 488 nm and 530 nm, respectively. The anisotropy (r) was calculated using the formula

$$r = \frac{I_{VV} - GI_{VH}}{I_{VV} + 2GI_{VH}}$$

where grating factor, $G = \frac{I_{HV}}{I_{HH}}$, I_{VV} is vertical excitation vertical emission, I_{VH} is vertical excitation horizontal emission, I_{HH} horizontal excitation horizontal emission and I_{HV} is horizontal excitation vertical emission. The fraction of DNA bound, f_B was calculated from the equation, $f_B = (r - r_0)/(r_{max} - r_0)$, where 'r' is the observed anisotropy, r_0 is the initial anisotropy of the free DNA, and r_{max} is the anisotropy at saturation. The data was fitted to Hill equation using Origin 8.5 and dissociation constant (Kd) of the TDP1/DNA complex was determined.

Structural modeling of TDP1 dimethylation

The X-ray crystal structure of the N-terminally truncated TDP1 (amino acids 149-608,TDP1(Δ148)) in complex with a duplex DNA (PDB ID: 5NWA) (Flett et al., 2018) was used as the template to model di-methylation of the human TDP1 residues R361 and R586. The structural coordinates of amino acids R361 and R586 were replaced with those of symmetrical dimethylarginine (HETATOM code 2MR) in WinCoot (Emsley et al., 2010). Protein-DNA interactions were measured and visualized in PyMol. Structural figures were created using PyMol and Adobe Illustrator.

Alkaline COMET assays

DNA damage levels in TDP1$^{-/-}$ MEFs cells expressing FLAG-TDP1^{WT}, FLAG-TDP1^{R361K}, FLAG-TDP1^{R586K}, and vector control, or *PRMT5 KO* cells were compared by alkaline comet assays according to the manufacturer's protocol (Trevigen, Gaithersburg, MD) as described previously (Das et al., 2014, 2016; Rehman et al., 2018). Briefly, after drug treatment for the indicated times, cells were retrieved and mixed with low melting agarose and spread on a pre-warmed slide. The slides were immersed in lysis solution at 4°C for 1 h, rinsed with deionized water, then immersed in a 4°C alkaline solution (50 mM NaOH, 1 mM EDTA, and 1% dimethyl sulfoxide) for 1 h followed by electrophoresis at a constant voltage of 25 V for 30 min at 4°C. Thereafter neutralization was done in 0.4 M Tris-HCl (pH 7.5), dehydrated in ice-cold 70% ethanol for 5 min and air-dried. DNA staining was done with ethidium bromide (EtBr) (Sigma). TriTek Comet Score software (TriTek Corp, Sumerduck, VA) was used to score comet tail length for at least 25 cells. Statistical analysis of comet lengths was done using the Student *t*-test.

Cell survival assays

TDP1$^{-/-}$ MEF cells or PRMT5 knockout HCT116 cells (6×10^3) were seeded in 96-well plates (BD Biosciences, USA) and separately transfected with plasmid DNA (FLAG-TDP1^{WT}, FLAG-TDP1^{R361K}, FLAG-TDP1^{R586K}, or vector control) using X-tremeGENE^{HP} DNA transfection reagent (Roche) according to the manufacturer's protocol as described above. Cells (TDP1$^{-/-}$ cells or PRMT5 KO cells expressing TDP1 variants) were treated with CPT for indicated concentrations for 48 h. As described previously 3-(4,5-dimethylthiazol-2-yl)-2,5-diphenyl tetrazolium bromide (MTT) (Sigma) was used to assess cell survival (Das et al., 2014, 2016; Rehman et al., 2018). Plates were analyzed on Molecular Devices SpectraMax M2 Microplate Reader at 570 nm. The percent inhibition of viability for each concentration of CPT was calculated with respect to the control. Data represent mean values ± S.D. for three independent experiments.

QUANTIFICATION AND STATISTICAL ANALYSIS

All statistical analyses were performed using GraphPad Prism 8 or Origin 8.5 software unless otherwise specified. The sample size and type of statistical test used are indicated in figure legends. All data are representative of 3 independent experiments unless otherwise stated. A p value of $p < 0.05$ was considered statistically significance.

Cell Reports, Volume *39*

Supplemental information

Interplay between symmetric arginine dimethylation and ubiquitylation regulates TDP1 proteostasis for the repair of topoisomerase I-DNA adducts

Sangheeta Bhattacharjee, Ishita Rehman, Saini Basu, Souvik Nandy, Julia M. Richardson, and Benu Brata Das

The interplay between symmetric arginine dimethylation and ubiquitylation regulates TDP1 proteostasis for the repair of topoisomerase I-DNA adducts

Sangheeta Bhattacharjee[1,3], Ishita Rehman[1,3], Saini Basu[1], Souvik Nandy[1], Julia M. Richardson[2], and Benu Brata Das[1, 4, *]

[1]Laboratory of Molecular Biology, School of Biological Sciences, Indian Association for the Cultivation of Science, 2A & B, Raja S. C. Mullick Road, Jadavpur, Kolkata-700032, INDIA.

[2]Institute of Quantitative Biology, Biochemistry, and Biotechnology, School of Biological Sciences, University of Edinburgh, The King's Buildings, Max Born Crescent, Edinburgh, EH9 3BF, UK.

[3]These authors contributed equally

[4]Lead contact

*Correspondence: pcbbd@iacs.res.in (BBD)

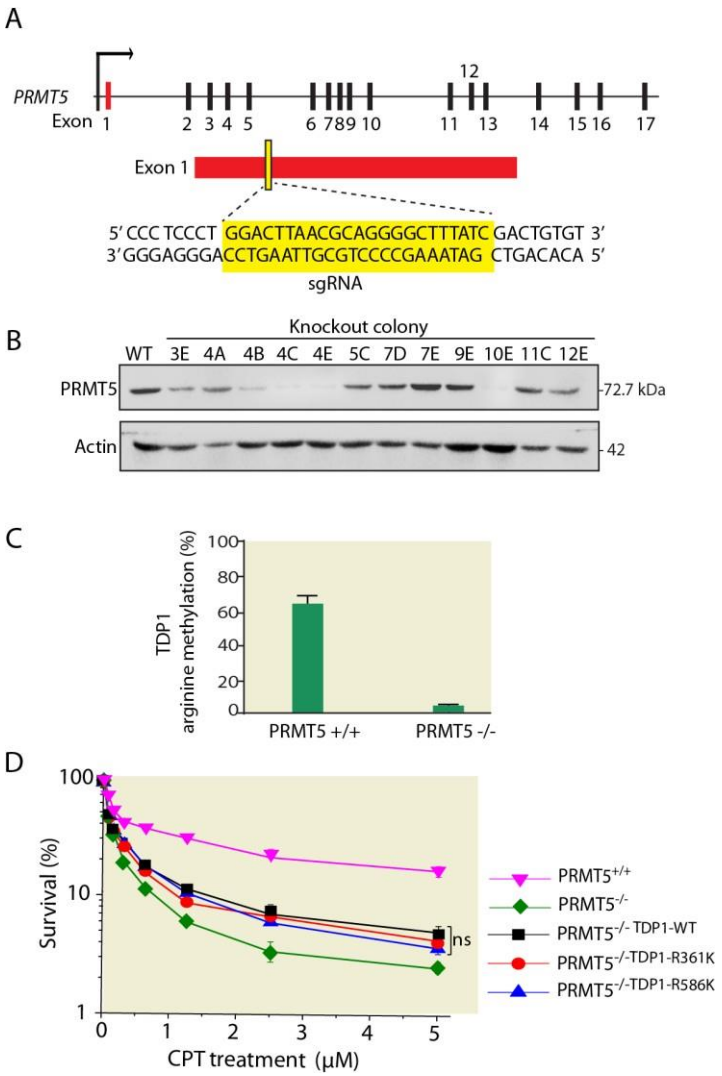

Figure S1. Characterization of PRMT5 knockout cells, Related to Figure 1.

(A) Validation of CRISPR-Cas9 mediated knockout cell line. Schematic representation of PRMT5 gene targeted by sequence-verified guide RNA. (B) Western blot showing PRMT5 protein levels in wild-type (WT) and single cell expanded clones. Colony 10E was used for PRMT5 KO clonal expansion. β-actin level is shown as a loading control. (C) Densitometry analysis of TDP1 symmetric arginine methylation level. TDP1 arginine methylation was quantified and normalized to FLAG-TDP1 (Figure 1A) and represented as fold change. Error bars represent mean ± S.E. (n = 3). (D) Cell survival curves of *wild-type* (PRMT5$^{+/+}$), *PRMT5*

KO (PRMT5$^{-/-}$), and *PRMT5 KO* cells complemented with FLAG-tagged TDP1 variants (PRMT5$^{-/-\text{TDP1 WT}}$, PRMT5$^{-/-\text{TDP1 R361K}}$ and PRMT5$^{-/-\text{TDP1 R586K}}$) when exposed to CPT for 72h. CPT-induced cytotoxicity (%) was calculated with respect to untreated cells. Each point corresponds to the mean ± S.D. of at least three experiments. Error bars represent SD (n= 3; ns, p>0.05; t-test).

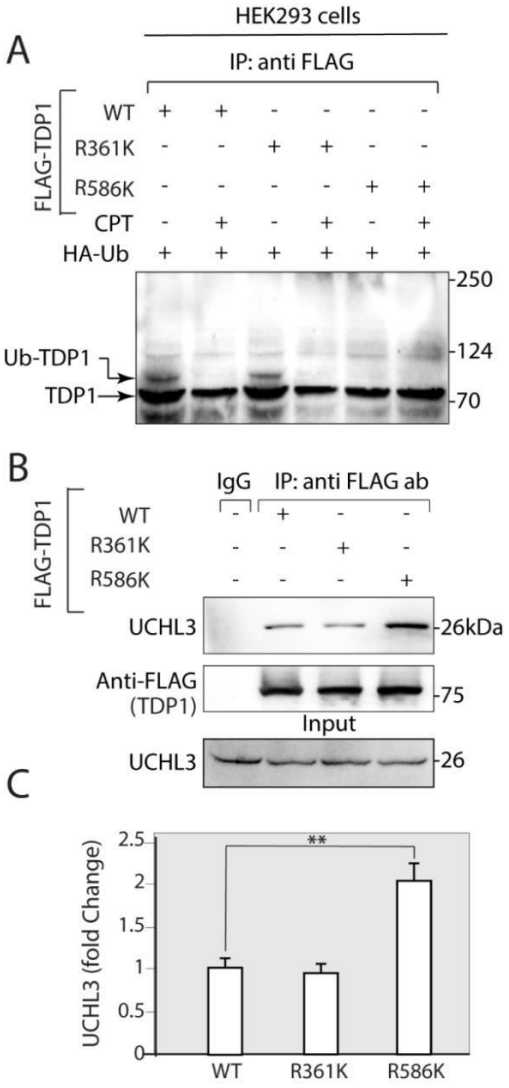

Figure S2. TDP1-R586 methylation promotes Ubiquitin/Proteasome-dependent turnover, Related to Figure 3.

(A) R586 dimethylation promotes TDP1-Ubiquitylation in the HEK293 cell line. FLAG-tagged TDP1 constructs: wild-type (WT), single arginine dimethylation mutants (R361K), or (R586K) and HA-Ubiquitin were co-transfected in HEK293 cells, in the absence or presence of CPT (5 μM, 3 h). FLAG-TDP1 variants were immunoprecipitated using an anti-FLAG antibody and the immune complexes were blotted with the anti-FLAG specific antibody to detect TDP1 species. The slowly migrating ubiquitylated TDP1 (Ub-TDP1) is indicated. Migration of protein molecular weight markers (kDa) is indicated at right. (B) R586 dimethylation blocks binding with UCHL3 (Deubiquitylase, DUB). FLAG-tagged TDP1 constructs: Wild-type (WT), single arginine dimethylation mutants (R361Kor R586K) were ectopically expressed in HCT116 cells. FLAG-TDP1 variants were immunoprecipitated using an anti-FLAG antibody and the immune complexes were blotted with an anti-UCHL3 specific antibody (representative experiment) and quantified by densitometry (panel C) normalized against UCHL3 (input). Aliquots (10 %) of the input show the level of UCHL3 before immunoprecipitation. Data represent the mean ± S.E. values of independent experiments. Asterisks denote statistically significant differences (**$P<0.001$; t-test).

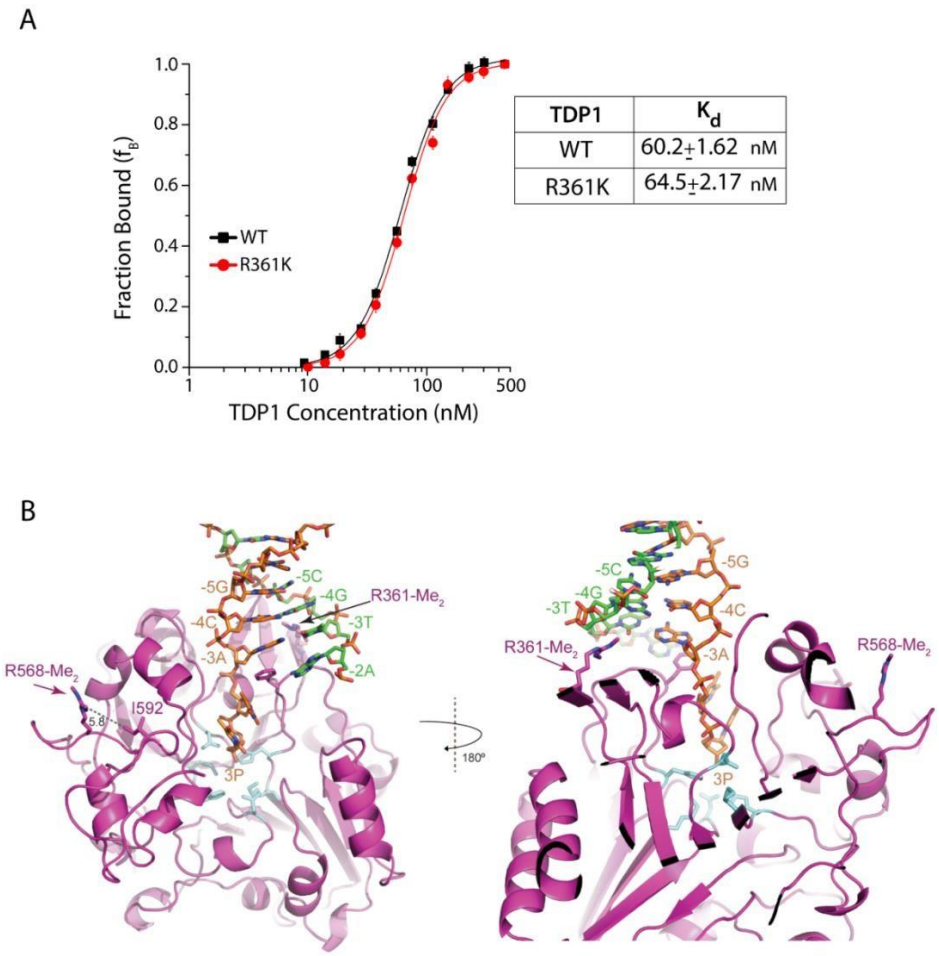

Figure S3. Structural impact of TDP1 symmetric dimethylation, Related to Figure 5.

(A) DNA binding assay by fluorescence anisotropy of dsDNA (HEI41-3P) as a function of recombinant TDP1 concentration (wild-type–WT; and TDP1methylation mutant at R361K). Anisotropy titration was performed using 10 nM 5’ 6-FAM labeled double-stranded DNA with a 3'phosphate. The anisotropy values were converted to the fraction of DNA bound using the formula mentioned in materials and methods and data was fitted to Hill equation using Origene software and dissociation constant (K_d) calculated. (B) Spatial arrangement of dimethylated arginines with respect to DNA. Front and back views of the structural model of TDP1, dimethylated at both R586 and R361, in complex with duplex DNA. TDP1 is colored purple and the dimethylated arginines are labeled. The scissile DNA strand is mustard and its 3'-phosphate

(labeled 3P) is close to the catalytic amino acids, shown as cyan sticks. The complementary DNA strand is green. The dotted black line indicates the shortest distance (in Å) between R586-Me_2 and I592.

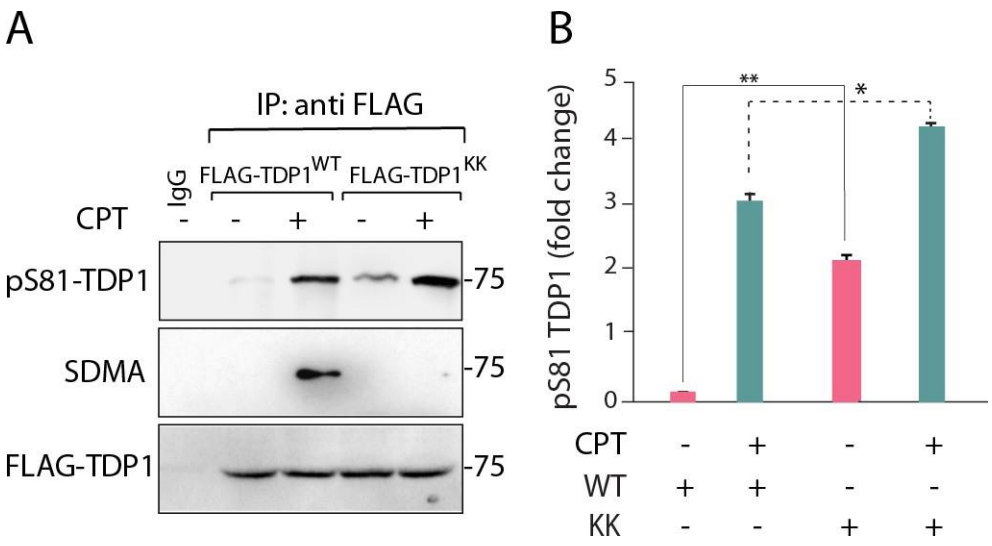

Figure S4. CPT-induced DNA damage increased TDP1 stability independently of TDP1-arginine methylation, Related to Figure 3.

Interplay between DNA damage-induced TDP1-S81 phosphorylation and TDP1 arginine methylation (A) FLAG-TDP1 *wild type* (FLAG-TDP1^{WT}) and TDP1 double-mutant for arginine methylation sites R361K and R586K [KK] (FLAG-TDP1^{KK}) were ectopically expressed in HCT116 cells in the presence and absence of exogenous DNA damage (CPT; 5µM, 3 h). FLAG-TDP1 variants were immunoprecipitated using anti-FLAG antibody and the immune complexes were blotted with the anti-pS81-TDP1 (Das *et al EMBO J*, 2009) and anti-SDMA specific antibodies (representative blot). The same blot was stripped and re-probed with an anti-FLAG antibody to show equal loading. Migration of protein molecular weight markers (kDa) is

indicated at right. (B) Densitometry analysis of CPT-induced TDP1-S81 phosphorylation level. pS81-TDP1 was quantified and normalized to FLAG-TDP1 and represented as fold change. Error bars represent mean ± S.E. (n = 3). Asterisks denote statistically significant differences (*P<0.01; **P<0.001; t-test).

Table S1. Related to STAR Methods. List of oligonucleotides used

Assay Type	Name	Sequence	Length(nt)
Real Time PCR	Actin	5′ Forward: GACCCAGATCATGTTTGAGACC 5′ Reverse: CATCACGATGCCAGTGGTAC	22 20
Real Time PCR	TDP1	5′ Forward: GACGTGGACTGGCTCGTAAA 5′ Reverse: GAGCCTTAGCCTCTCGCTTATC	20 22
Fluorescence based Ex-vivo assay	ssDNA (HEI40)	56-FAM/AGA GGA TCT AAA AGA CTT/3BHQ	18
Fluorescence based Ex-vivo assay	dsDNA (HEI50)	56-FAM/AAG TCT TTT AGA TCC CTC CGG ATC TAA AAG ACT T/3BHQ	34 (15 nt hairpin)
Fluorescence anisotropy	(HEI41-3P)	56-FAM/AGA GGA TCT AAA AGA CTT-3P	18
Fluorescence anisotropy	(HEI41-C)	5′ AAGTCTTTTAGATCCTCT 3′	18 (complement)